Experimental behaviour of aeronautical notched carbon fibre reinforced thermoplastic panels under combined tension-shear-pressure loadings

Florent Grotto, Christophe Bouvet, Bruno Castanié, Joël Serra

Journal Pre-proofs

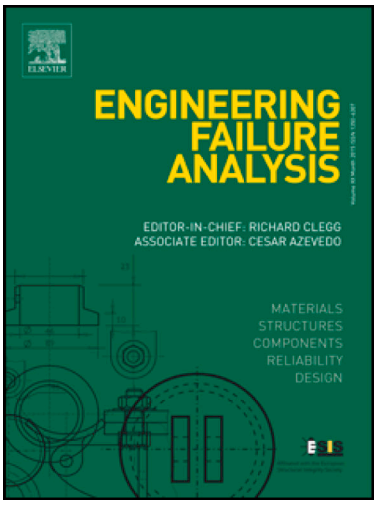

Experimental behaviour of aeronautical notched carbon fibre reinforced thermoplastic panels under combined tension-shear-pressure loadings

Florent Grotto, Christophe Bouvet, Bruno Castanié, Joël Serra

PII: S1350-6307(23)00029-8
DOI: https://doi.org/10.1016/j.engfailanal.2023.107075
Reference: EFA 107075

To appear in: *Engineering Failure Analysis*

Received Date: 18 October 2022
Revised Date: 2 January 2023
Accepted Date: 16 January 2023

Please cite this article as: Grotto, F., Bouvet, C., Castanié, B., Serra, J., Experimental behaviour of aeronautical notched carbon fibre reinforced thermoplastic panels under combined tension-shear-pressure loadings, *Engineering Failure Analysis* (2023), doi: https://doi.org/10.1016/j.engfailanal.2023.107075

Experimental behaviour of aeronautical notched carbon fibre reinforced thermoplastic panels under combined tension-shear-pressure loadings

Florent Grotto [a], Christophe Bouvet [a], Bruno Castanié [a] and Joël Serra [a]

[a] Institut Clément Ader (UMR 5312), ISAE-SUPAERO – INSA – IMT Mines Albi – UPS – CNRS, Toulouse, France

* Corresponding author: castanie@insa-toulouse.fr

Abstract:

The demonstration of compliance of aeronautical structures with certification requirements is generally based on the building block approach, considering tests from the coupon level up to full-scale level. Coupon-scale tests are numerous and generally focused on uniaxial loading to target elementary failure modes, whereas structures are submitted to complex and combined loadings, leading to costly test campaigns on thousands of coupons. This paper considers intermediate-scale tests to study structural issues at element level. Thin flat samples (558 x 536 mm²) made of carbon fibre reinforced thermoplastic with a large, sharp central notch of 100 mm are considered. The VERTEX test rig is used to apply complex and combined loadings in tension, shear and internal pressure. Metrics are defined and computed to describe the multiaxial loading state and the failure scenario of the samples. Pressure addition clearly precipitates the first failure for shear tests but not for tension tests. With or without pressure, shear tests tend to show failure for lower equivalent fluxes than tension tests.

Keywords: Aeronautics, fuselage, thermoplastic carbon laminates, multiaxial testing, notched failure

Highlights:

- Various combinations of tension, shear and pressure are applied to notched panels
- Carbon reinforced thermoplastic plates are subjected to post-buckling tests
- The VERTEX test bench loads at intermediate-scale levels
- Force fluxes are computed from stereo-correlation measurements and the Plate Theory
- Several experimental criteria are considered to describe failure

1 Introduction

The aeronautical industry has been showing growing interest in Carbon Fibre Reinforced composites – particularly thermoplastics – in contrast to the thermoset resins that have prevailed during recent decades. Despite higher material and production costs, thermoplastics attract interest because of their their: recyclability [1] as regulations are expected to increase towards sustainability; very long shelf life; high fracture toughness [2], [3]; higher temperature use [4] or thermoforming capability [5]. They can also be used to manufacture “net shape” parts by overmoulding [6]. The failure behaviour of Carbon Fibre Reinforced Polymers (CFRP) is widely studied in the literature and some authors directly address the comparison between thermoset and thermoplastic matrices [7], [8].

The residual strength in presence of crack damage of CFRP structures is generally evaluated through the point-stress or similar methods in open-hole tests [8],[9],[10],[11],[12],[13], in which the holes are sometimes also referred to as "notches". The size effect of the hole size relatively to the sample width is widely documented in the literature but mostly focuses on small circular holes with diameters up to 50 mm. Other publications deal with sharp notches [14],[15],[16] which are more critical for large damage [17] and raise questions such as loading direction relatively to the damage and mixed mode fracture [18],[19]. The point-stress method is used as a simple criterion to evaluate a preliminary damage state at panel level (referred to as stable damage state). Nevertheless, the d_0 criterion-distance value depends on numerous parameters, such as layup, ply thickness, and material. It might not be representative of larger crack phenomenology as it is usually identified with coupon tests. In notch tests, coupons tend to fail directly and catastrophically, whereas, in larger samples, the crack propagates more progressively.

It is therefore of interest to study the specificities of the tolerance of composite structures to large damage, in order to properly size aircraft to resist appropriate load levels despite, for example, fuselage puncture after uncontained engine failure [20] (Figure 1). Such an in-flight incident can generate a large notch in the fuselage, which may be contained in a bay (skin alone between stringers and frames) or may cut through a stiffening member (frame or stiffener). To the authors' knowledge, only a few publications deal with this large notch issue (from 100 mm) and the question is always considered in association with large stiffened panels [21], [22], [23], [24], [25], [26]. These studies use simple uniaxial loading in tension or compression, while other types of study combine it with internal pressure to be more representative of the in-flight fuselage loading [27], [28], [29], [30]. The study, and especially experimental studies, of the combination of tension, shear and pressure loads on a large notch is original in the scientific literature.

Few test rigs in the world can achieve complex loadings on structural elements. A first type of machine introduces loads to the sample directly from attached actuators (Figure 2). A few actuators are used to load samples of approximately one square metre [31], [32], [33] but larger tests are more complex, with the use of many actuators to generate compression/shear [34]. Another type of machine exists, where loads are not introduced directly into the sample from the actuators but, instead, the sample is part of a larger structure, itself loaded by actuators [35], [36], [37], [38]. Several types of loading can be applied to the structure simultaneously (tension/bending/torsion), generating combined complex

loading within the sample. The loadings obtained from this type of structure-embedded configuration to derive design values are assumed to be more representative of actual loadings.

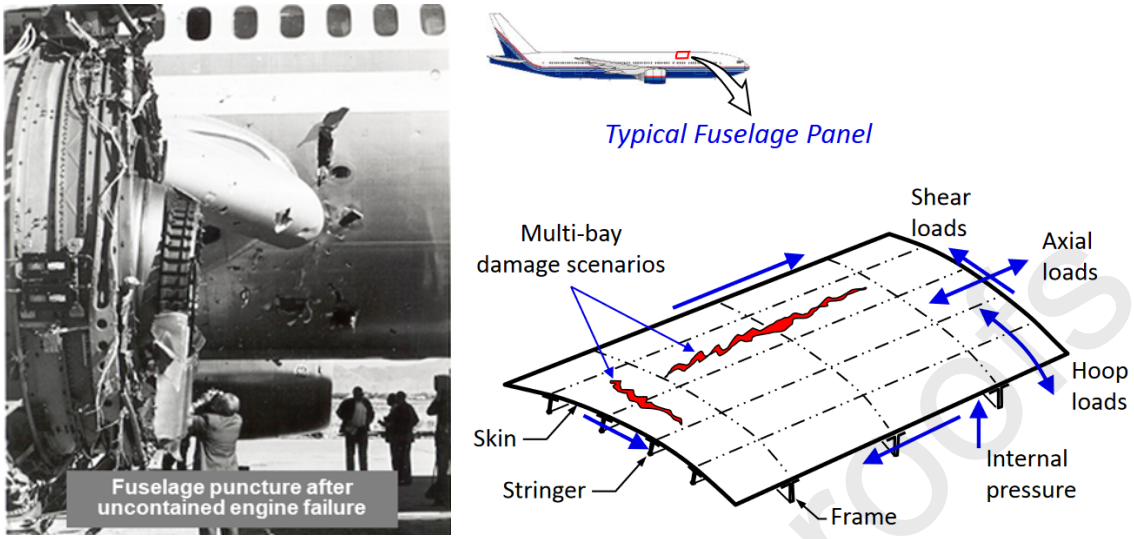

Figure 1: Large damage on fuselage generated by uncontained engine failure (left [39], right [40]).

A limited number of test rigs around the world allow large samples to be tested under complex or even combined loads and such tests at the top of the test pyramid [41] (Figure 3) are costly. The VERTEX test rig positions itself in the intermediate scale of the test pyramid, between coupons and components. Serra et al. [42] presented the machine and the state of the art for this kind of intermediate multi-axial test rigs. Large notch behaviour [43] and residual strengths post impact [44] have been assessed for planar samples under combined loadings. This is a first step towards moving up one level of the test pyramid with stiffened samples to finally assess large damage behaviour phenomenology, representative of current fuselage sections, at moderate cost.

The aim and originality of the present study is to study large notches, on a thermoplastic CFRP panel, at the element scale and under structural complex combined loadings: in tension, shear and pressure. The first part of the paper presents the working principle of the VERTEX test rig and the full-field measurement setup to monitor the combined pressure-tension-shear tests. Metrics are defined and computed to describe the loading state of the elements tested and to discuss the structural testing itself. Failure metrics are also considered to assess the effects of pressure and loading multi-axiality on the notch propagation.

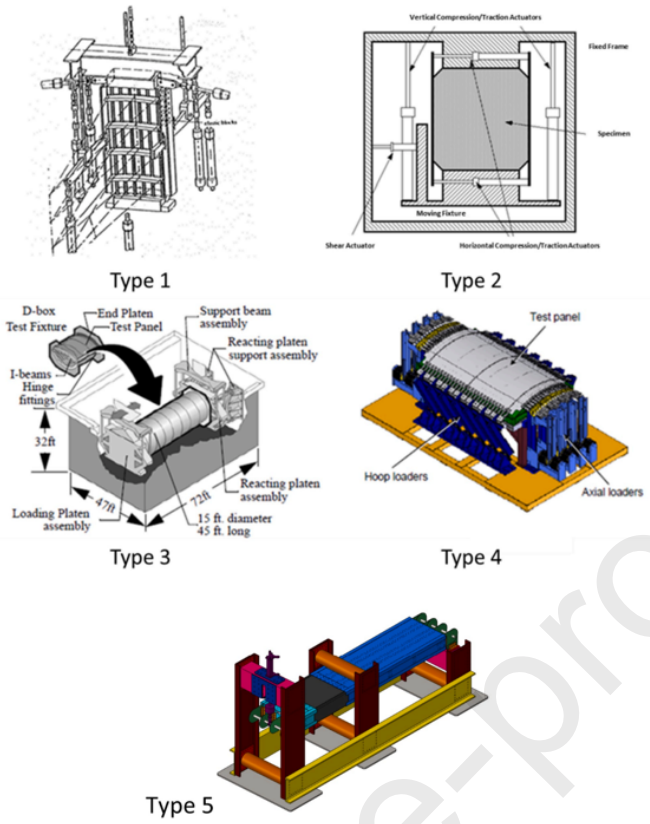

Figure 2: Complex loading test rigs identified by [44] (extracted from [45] for type 1, [46] for type 2, [47] for type 3, [48] for type 4, [49] for type 5).

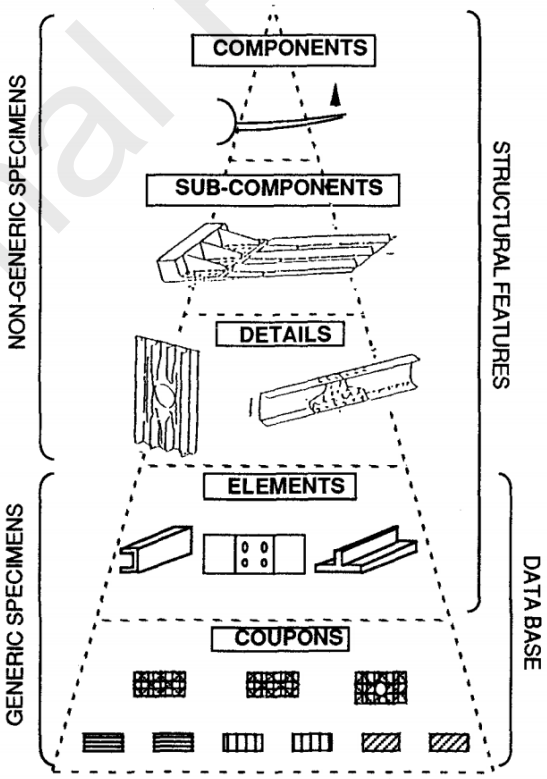

Figure 3: The pyramid of tests [41] representing the numerous small mechanical tests providing a design basis for the fewer and larger tests.

2 Materials and methods

A single specimen geometry was considered for this study (Figure 4 and Figure 5). It comprised a 558 mm × 536 mm plane plate with 128 holes to bolt the specimen to the test bench, which left a useful zone of 400 mm × 400 mm. A single quasi-isotropic stacking sequence of $[+45; -45;90; 0]_s$ was used for carbon-thermoplastic prepreg (unidirectional carbon fibres and thermoplastic matrix). For confidentiality reasons, the material properties, the thickness and the manufacturing process cannot be disclosed in this article. All forces and strains are also normalised to respect confidentiality.

The edges, the holes and a 100 mm centre-notch were milled to keep the ratio W/L = 4 and the maintain representativeness of large damage phenomenology. The notch was machined with a 2 mm mill to keep the manufacturing process simple and reproducible for thicker specimens. This process left an end notch radius of 1 mm. It should be noted that the end notch geometry was expected to have a limited effect on failure initiation and even less on further propagation [50].

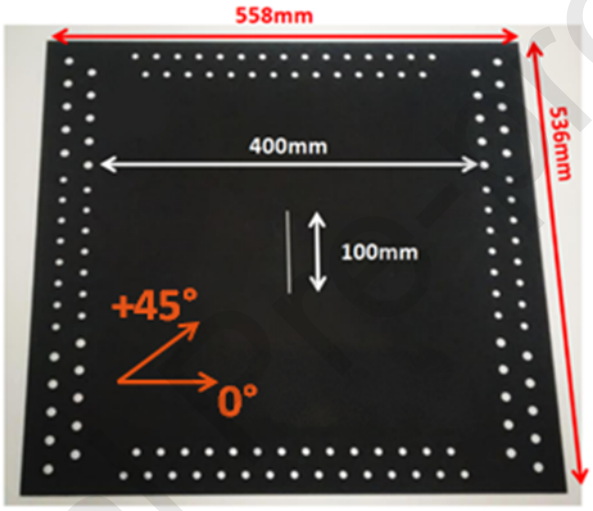

Figure 4: Notched VERTEX specimen geometry.

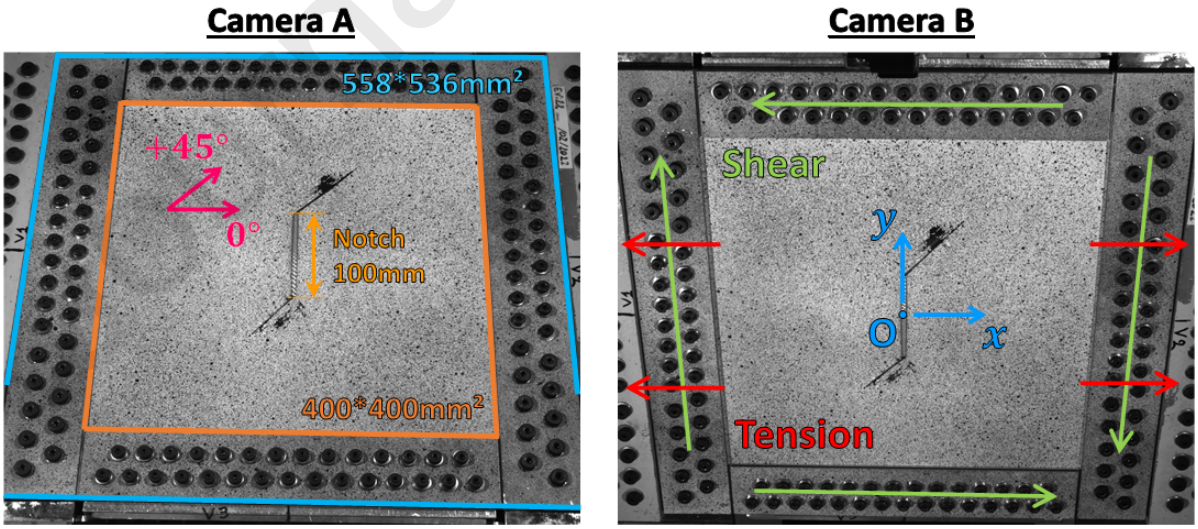

Figure 5: Plate sample geometry and directions on the VERTEX test rig, viewed using both optical cameras for digital image stereo-correlation (5 Mpx, 2 fps), during crack propagation.

2.1 Specimen manufacturing

The specimen was a flat drilled plate, without over-thickness under the tabs to avoid adding complexity to the manufacturing process. The hand lay-up process of this thermoplastic prepreg plies was very similar to that for usual thermoset materials, except that raw plies did not stick to each other, making it difficult to keep the relative positioning of plies. However, thermoplastics can be welded, so consecutive plies were held together by pressing a soldering iron on the current top ply (welding points mostly on the borders and some in the centre). This method was assumed not to be intrusive since the full consolidation cycle would later re-melt the thermoplastic resin and re-crystallise it properly.

According to the manufacturer's processing guidelines, this thermoplastic material has to be consolidated at high pressure and high temperature (above 300 °C). Since a heating press and a mould were chosen to apply this consolidation, such high temperatures were likely to generate significant stresses in the consolidated plate and the mould itself because of the relative difference of thermal expansion of the composite and the mould material. Therefore, a specific mould was made of INVAR material (Fe-Ni36%) that had a thermal expansion coefficient closer to that of the composite than those of the usual metallic materials, thus reducing possible manufacturing defects [51].

DSC (Differential Scanning Calorimetry) analyses were carried out on samples taken from a few manufactured plates. The measured average crystallinity of the resin was found to match the upper value of the crystallinity range recommended by the manufacturer. In addition, Choupin et al. [52] showed relatively low sensitivity of the mechanical properties to the crystallisation rate on Poly-Ether-Ketone-Ketone thermoplastics: the crystallinity measured therefore supports the validity of the manufacturing process and rules out any major deviation of the mechanical properties of the resin.

2.2 VERTEX test rig

The VERTEX test rig (Figure 6 and Figure 7) used in this study was developed from a previous, similar machine [53],[54] and was first used by Serra et al. [42]. The machine is mainly made up of a tubular box on which the specimen is bolted to complete the upper face of the central part. Jacks 1 and 2 can be pushed or pulled symmetrically to bend the box, locally creating tension or compression on the sample. Jacks 3 and 4 can be pushed to twist the centre of the box, locally creating shear on the sample. An air-pressurised rubber bladder (Figure 8) can be added in the central box to load the sample with pressure. The four jacks and the bladder pressure can be controlled independently to apply combined structural loadings in tension/compression + shear + pressure on the sample.

The rubber bladder is wrapped inside a large sheet of aramid fabric, to protect the bladder from carbon splinters coming from the sample and to restrain potential blasts. The bladder applies a pressure uniformly on the lower skin of the sample, on a 380 mm × 380 mm centred square that is most of the area of interest. The bladder is inflated by compressed air using a "valve + regulator + filter + safety valve" system, connected to the building's compressed air network. The circuit is equipped with an overpressure safety valve so as not to damage the bladder by excessive inflation. The pressure is manually monitored to maintain the constant value desired through the duration of the test.

In contrast to the situation during uniaxial coupon testing, it is generally not possible to directly know the load passing through the specimen from the displacements and forces of the remote actuators. Cameras overhang the sample (Figure 9) to take full-field measurements: two optical cameras focus on the entire area of interest (Figure 5) and an infrared camera is used to detect composite failures through their heat dissipation [55] (Figure 10). Using thermal emissivity differences and local surface orientations, various components (sample, tabs, notch, bolts) can be identified in thermography even if they have the same actual temperature. The optical cameras and the speckle painted on the samples enabled stereo-correlation to be performed with the commercial software VIC-3D 7, using a local subset method (subset=29 px; step=7 px; filter=15 px; 1 px $\approx$ 0.28 mm).

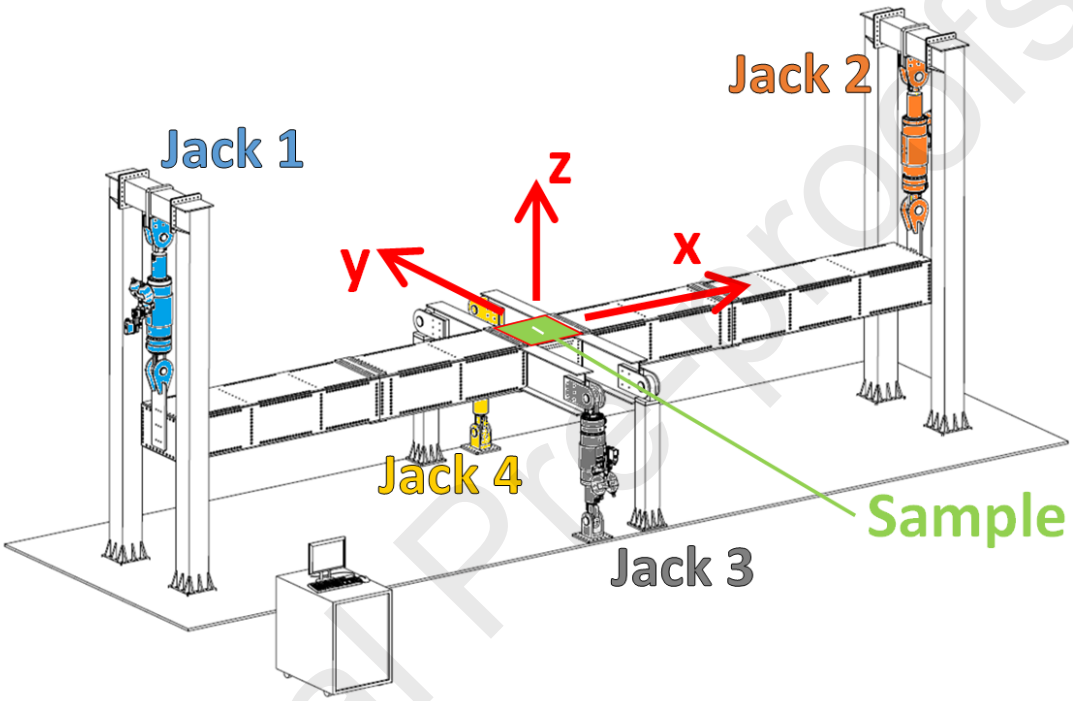

Figure 6: Scheme of the VERTEX test rig and its four jacks to load the sample placed in the middle.

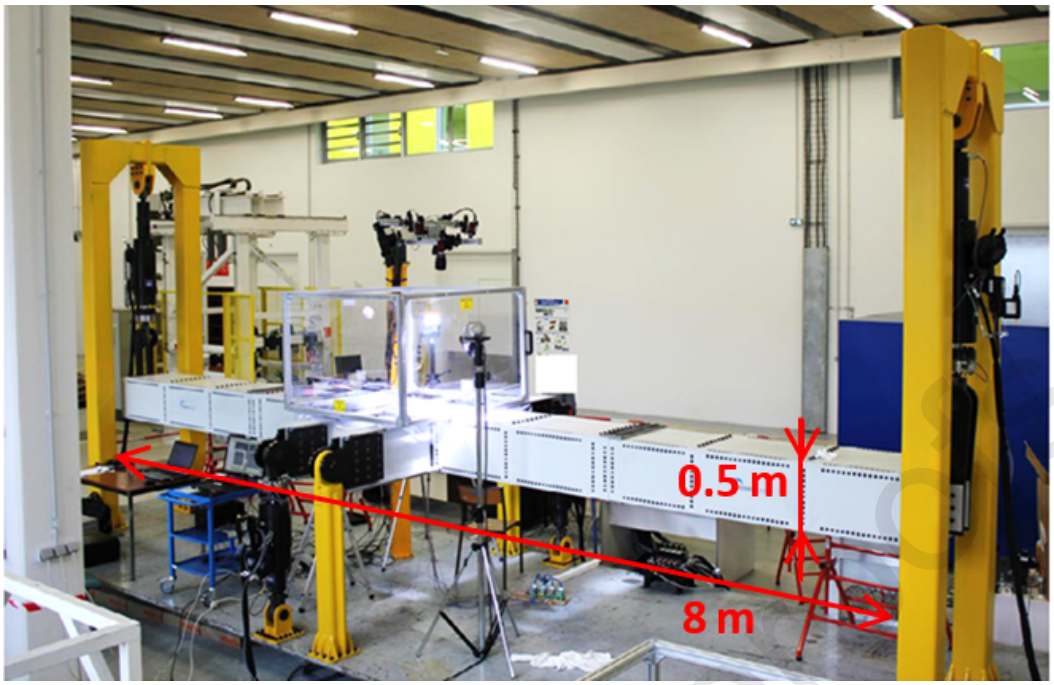

Figure 7: Picture of the VERTEX test rig.

Figure 8 : Rubber bladder positioned inside the yellow pressure chamber, itself placed in the central box of the main beam of the VERTEX test rig. The sample is bolted on top of it, thus closing the upper face of the pressure chamber.

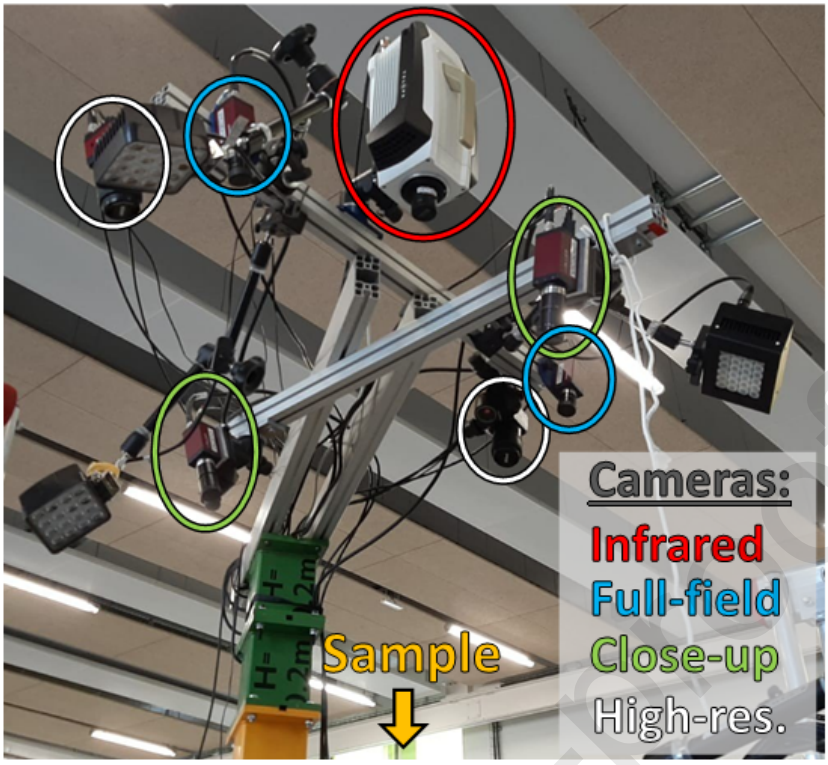

Figure 9: Instrumentation by cameras looking down on the sample – only the infrared camera and the two optical full-field cameras are considered in this study.

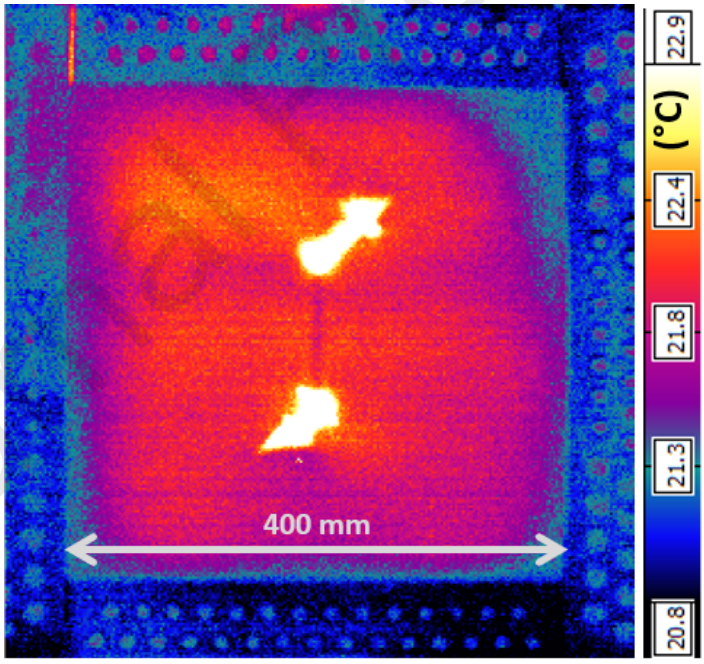

Figure 10: Thermography of the sample from the infrared camera (320×256 px, 100 fps), taken simultaneously with frames of Figure 5.

2.3 Test matrix

Table 1 indexes the six tests performed in this study. Tension and shear were used as reference loadings and a single tension + shear test was performed to browse the combined loading space of tension and shear. The same three tests were repeated with pressure in order to be able to analyse the effect of pressure combination. The internal pressure was applied to most of the area of interest, before the tension/shear loading, and remained constant during the test. The initial pressure (confidential value) applied at the beginning of the tests was representative of an aircraft in-flight pressure differential.

Loads were applied up to propagation of a major crack, generally until the crack reached one side of the specimen, because, when a sample is broken, the load continues to go through the rest of the bench and can damage it.

Test reference	Loading
T^0_{tens}	Tension
T^0_{shear}	Shear
$T^0_{tens+shear}$	Tension + Shear
T^{pres}_{tens}	Tension + Pressure
T^{pres}_{shear}	Shear + Pressure
$T^{pres}_{tens+shear}$	Tension + Shear + Pressure

Table 1: Test matrix considered.

3 Results

After observation of the general test features, this section focuses on the definition of metrics to evaluate the general failure state of the specimen. Other relevant metrics are also defined to describe the nature and intensity of loading states, in order to discuss tests individually and comparatively despite their different natures. The mechanical interpretations of graphs obtained with these metrics are mostly given in the next section, where all the elements necessary for the discussion are gathered together.

3.1 Direct observations

3.1.1 Overall displacement fields

Figure 11 shows typical in-plane displacements and the out-of-plane shape obtained from the two optical cameras by stereo-correlation (Figure 5), using speckles painted on the upper face of the sample. The reference image taken for displacements was that of the free sample simply laid down on the VERTEX bench, i.e. before clamping by bolting of the 128 holes of the sample. Because of manufacturing defects like spring-back and out-of-plane deflexions due to clamping, the initial shapes of samples were slightly curved by a few millimetres. Therefore, to estimate the buckled shape, it was preferable to look at Z out-of-plane position than at W displacement since the relative displacement was affected by the curvature of the reference shape. Amplitudes of fields ΔU,ΔV,ΔZ along the x,y,z directions are given to enable the relative amplitude of fields to be appreciated in each direction. Note that out-of-plane displacements are much greater than in-plane displacements because of the early buckling during the tests.

Observed fields of U and V displacements are irregular as, for example, they are not uniform on sides that are far from the notch. Such production of uneven fields is an asset of the structural testing of the VERTEX test bench built from closed sections, as it should be more representative of loads acting on an aircraft fuselage section. For tension, the useful U field shows displacement concentrated in the centre of the left and right edges, whereas ideal tension would impose constant displacements over these edges. Longitudinal tension is also accompanied by transverse compression of similar amplitude at sub-millimetre scale displacements (as V displacements are oriented towards the centre). For shear, the U and V displacements are, respectively, quite symmetrical for the load considered and not constant on the four edges. The pattern of the -45° buckle can be observed in the in-plane displacement fields because of the significant out-of-plane rotations.

Figure 12 shows 3D shapes and amplitudes of the sample for: clamping only, pressure, and the six loading conditions considered. The three tests without pressure show upward mode I buckle shapes, oriented from 0° to -45° depending on the proportions of tension and shear. The clamping of the sample (bolting of the 128 holes of the sample to the bench) constrains the sample enough to cause it to buckle before any useful load is applied. The pressure applied after clamping imparted a large, symmetric, out-of-plane displacement that smoothed any further buckle shape of the following tests with pressure.

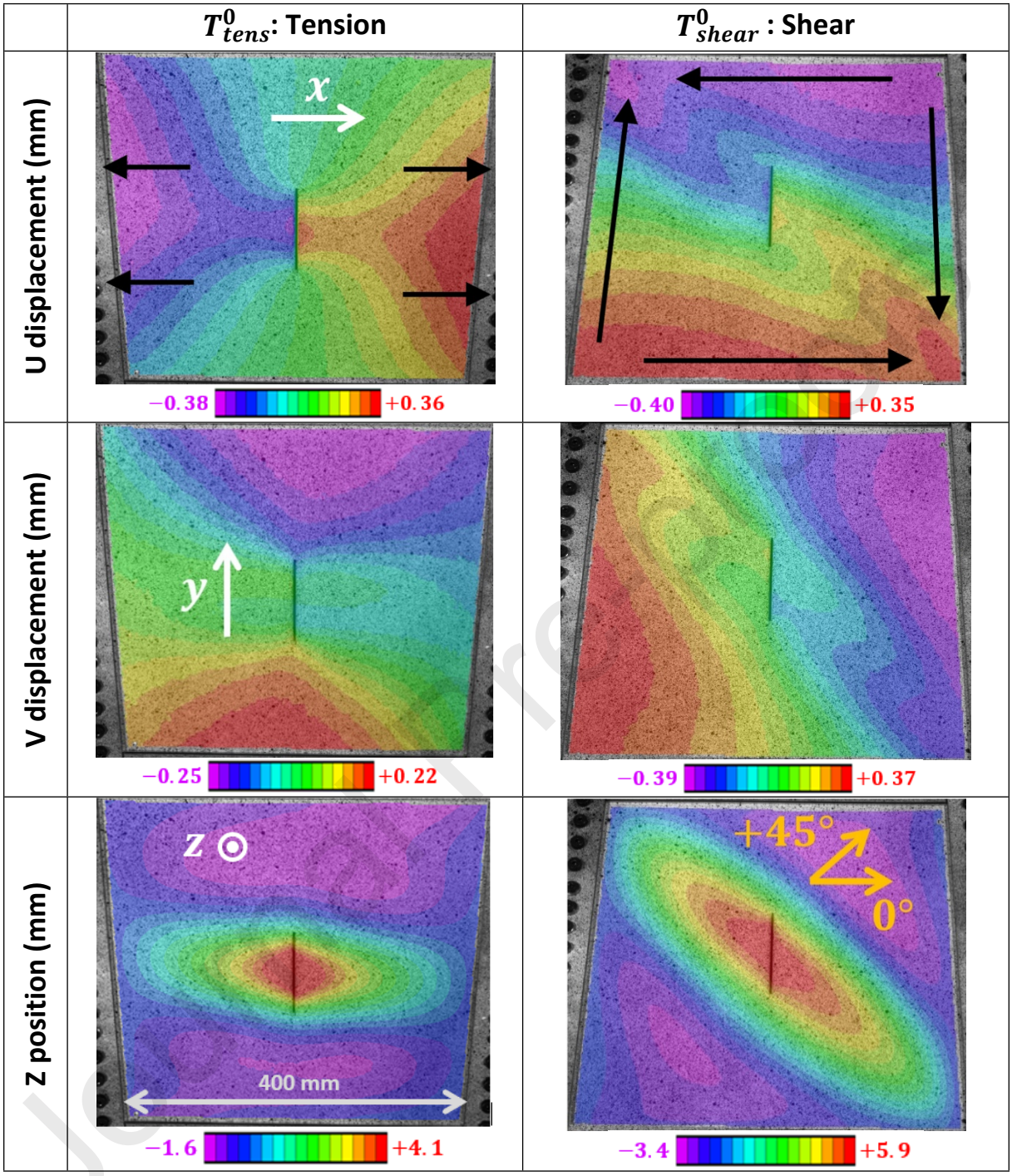

Figure 11: Fields of in-plane displacements and out-of-plane position, of tension and shear tests before failure, computed through stereo-correlation on the 400 mm × 400 mm useful zone.

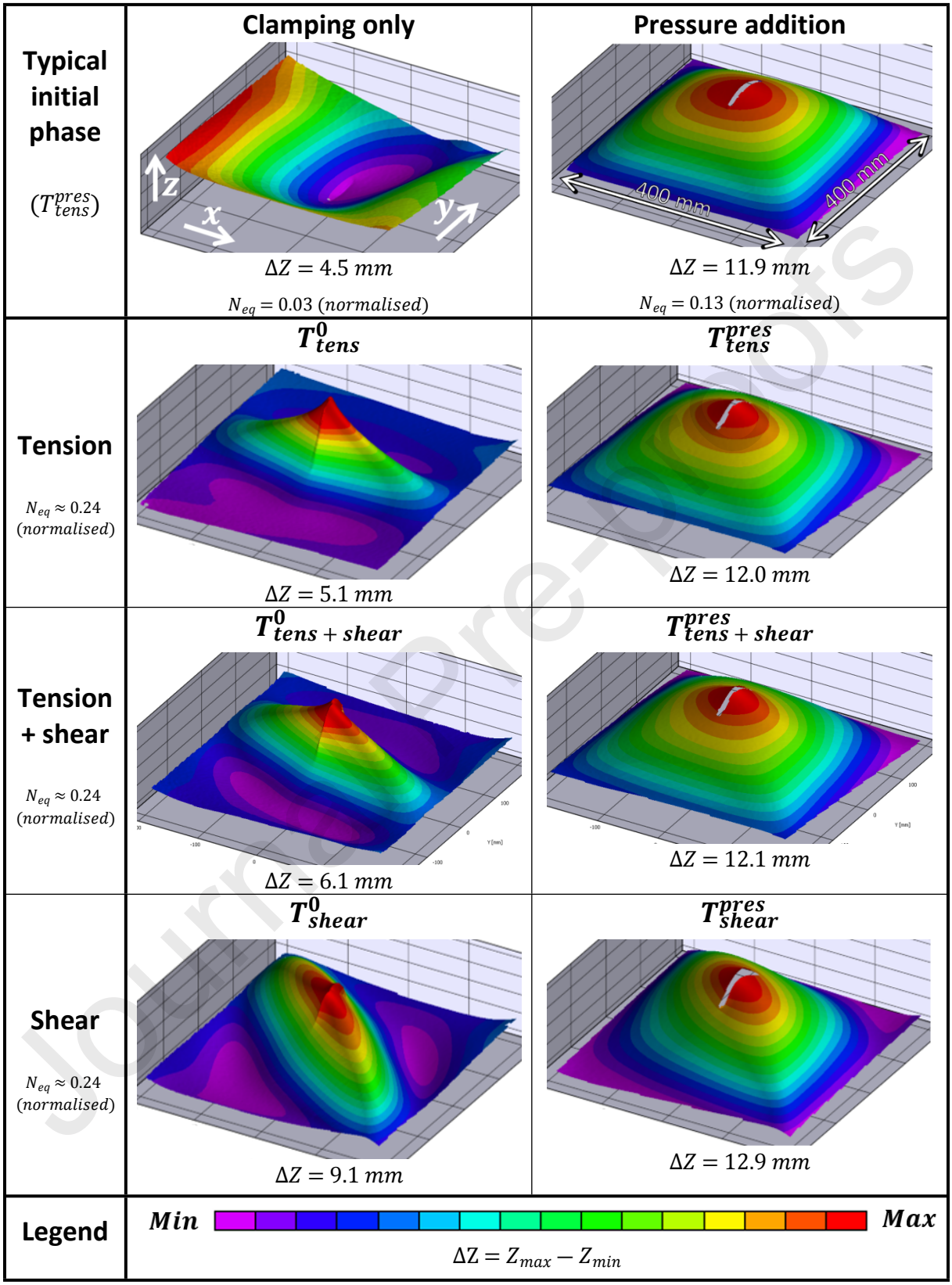

Figure 12: Out-of-plane exaggerated 3D shapes before crack propagation: typical initial phase and comparison of tests without and with pressure for the same equivalent flux (defined below), given by VIC-3D from the stereo-correlation on the 400 mm × 400 mm useful zone.

.

3.1.2 Failure patterns

Thermographs obtained with the infrared camera (Figure 10) show local heating caused by composite damage events. The thermal signals observed came mainly from fibre failures, which dissipated far more energy than other failure modes (matrix cracking or delamination). Infrared frames had a low resolution of 320 × 256 px, which was nevertheless enough to detect failure signals, and the camera was set to 100 frames per second to be able to differentiate failure propagation directions and the chronology of failure occurrences. Following each damage event detection, its heat is propagated, blurring the thermography.

Figure 13 shows failure patterns for each test without pressure (tests with pressure gave very similar failure patterns), measured by the infrared camera after a given main failure and from the optical camera perspective at the end of the test (since thermographs were blurred at the end of the test). As intended, failure patterns of the optical images directly match the ones observed clearly with infrared images. Infrared measurements allowed fibre failures to be detected even if they were confined in the central plies or were located on bottom plies (opposite side of the sample), as the heat generated by fibre failures propagates quickly through the thickness of the sample. For example, the corner failure of the shear test T^0_{shear} (see top-left corner of the corresponding infrared image shown in Figure 13) can be detected with the infrared camera despite the fact that post-mortem observations indicated that it was confined to the bottom plies. Note that the tests were stopped before complete failure of the specimen, to avoid any subsequent damage to the test bench.

Firstly, cracks along the +45° and -45° direction matched failures of fibres along opposite directions, respectively -45° and +45°. The tension tests T^0_{tens} and T^{pres}_{tens} showed a crack propagation along the +45° direction with tension fibre failures, whereas shear tests T^0_{shear} and T^{pres}_{shear} mostly propagated along the -45° direction with compression fibre failures. Hence, the tension-shear tests $T^0_{tens+shear}$ and $T^{pres}_{tens+shear}$ gave more complex directions of cracks.

Secondly, previous tests on similar thermoset samples [43] gave simpler failure patterns since:

- Tension tests cracks propagated essentially along the 90° direction for thermoset samples, as expected for brittle failure of carbon fibres, but deviation from 0° in the thermoplastic samples was probably due to the different layup
- Unlike in T^0_{shear}, $T^0_{tens+shear}$ and T^{pres}_{shear} tests, cracks rarely forked in thermoset samples
- Main final failures were brutal and easy to identify for thermoset samples, whereas current thermoplastic samples gave more progressive failures

Test reference	Optical image of failure	Infrared image of failure (°C)
T^0_{tens} Tension	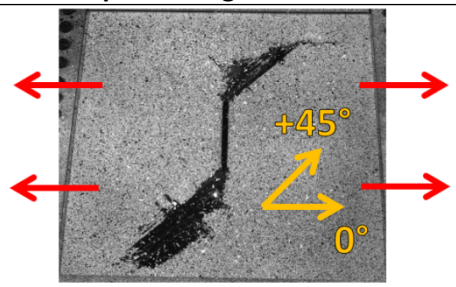	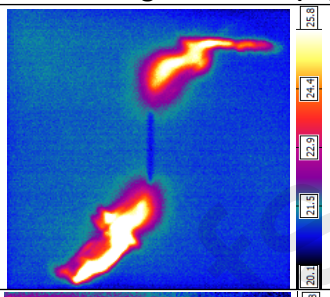
T^0_{shear} Shear	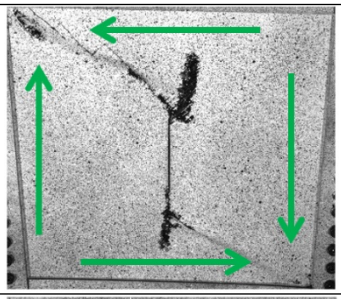	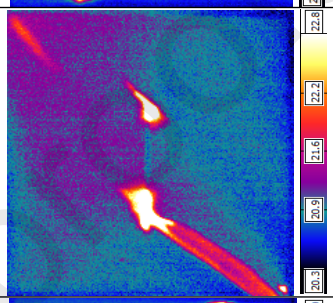
$T^0_{tens+shear}$ Tension + shear	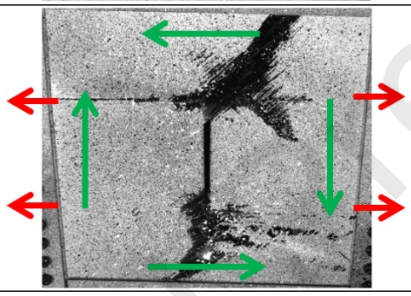	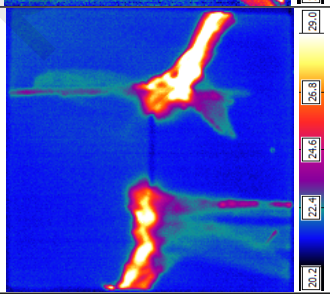

Figure 13: Failure patterns on tests without pressure, from optical camera images at the end of the test and from the infrared camera images after a given main failure (arbitrary scale) – focus on the 400 mm ×400 mm useful zone.

3.2 Method to compute force and moment fluxes

Structural panels are usually sized using plate force fluxes (N_x,N_y, T_{xy}) and moment fluxes (M_x,M_y,T_{xy}): they represent loads and moments per unit of length (respectively *N/mm* and *N*) and are independent of the laminate thickness. Using the classical plate theory [56] and full-field measurements of the stereo-correlation, Equation 1 and Equation 2 show how plate fluxes can be computed from: upper-skin strain measurements, out-of-plane displacement measurements and the assumed stiffness of the plate. The latter is computed from confidential ply thicknesses, layup, and ply material values of the carbon-thermoplastic considered.

Figure 14 shows all flux fields computed on most of the area of interest, with a 5 mm step between points. First, the stereo-correlation was performed with a local subset method, thus not allowing for proper measurements around borders and the notch: see blank zones in the plotted fields. Second, the flux computation is based on the calculation of second derivatives of W displacement with the

finite difference method, thus using neighbour point values, with a step of 5 mm. This method causes the blank zones to propagate by one step, reducing the domain of flux estimation. Note that the finite difference method is sensitive to noise and has an inherent averaging filter of the size of the step.

Therefore, flux fields give rich data to describe the load spatial distribution in the plate, except at the notch border and at the exterior border. Figure 15 presents another way to represent the spatial distribution of force fluxes, as is usually done for stress vectors in introductory mechanics courses. This vector representation allows the shape of loading to be visualised, in a more meaningful way than the three displacement fields.

A simple description of the temporal evolution of fluxes requires each spatial field to be aggregated into a representative scalar so that it can be plotted against time. For a given frame captured by cameras, flux fields are computed, then a scalar representative of border fluxes is computed for each field by averaging the flux values contained in the black boxes of Figure 14. The average fluxes over time are plotted in Figure 16 as an example and all further flux curves were obtained in this way. According to the classical plate theory, force and moment fluxes can be regularised [57] so that they can be compared on a common ground of stresses, with the membrane stresses and the flexural stresses on the top skin. Hence, in spite of the normalisation and the confidentiality of the thickness, the incidence of moment fluxes can be compared directly to that of the force fluxes, thanks to the factor $6/thickness$ [57] used in Figure 16. Force fluxes had 10 times the impact of moment fluxes at the end of the T^0_{shear} test ($N_x^{norm} \approx T_{xy}^{norm} = 0.4 \gg M_x^{norm} \times \frac{6}{thickness} = 0.04$); therefore, the contribution of moments can be neglected for failure considerations.

$$\underline{\underline{\varepsilon}}(M(x,y,z)) = \begin{bmatrix} \varepsilon_{0x}(x,y) \\ \varepsilon_{0y}(x,y) \\ \gamma_{0xy}(x,y) \end{bmatrix} + z * \begin{bmatrix} -\frac{\partial^2 w}{\partial x^2}(x,y) \\ -\frac{\partial^2 w}{\partial y^2}(x,y) \\ -2\frac{\partial^2 w}{\partial x \partial y}(x,y) \end{bmatrix}$$

curvature; height/2

Upper skin (measured) = membrane (deduced) + bending (upper skin) (computed)

Equation 1: Computation of membrane strains from upper skin measurements, assuming the classical plate theory.

$$\begin{bmatrix} N_x \\ N_y \\ T_{xy} \\ M_x \\ M_y \\ M_{xy} \end{bmatrix} = \begin{bmatrix} \underline{\underline{A}} & \underline{\underline{B}} \\ \underline{\underline{B}} & \underline{\underline{D}} \end{bmatrix} \cdot \begin{bmatrix} \varepsilon_{0x} \\ \varepsilon_{0y} \\ \gamma_{0xy} \\ -\frac{\partial^2 w}{\partial x^2} \\ -\frac{\partial^2 w}{\partial y^2} \\ -2\frac{\partial^2 w}{\partial x \partial y} \end{bmatrix}$$

Flux = Stiffness x plate strains

Equation 2: Computation of force and moment fluxes from the stiffness matrix and plate strains, according to the classical plate theory.

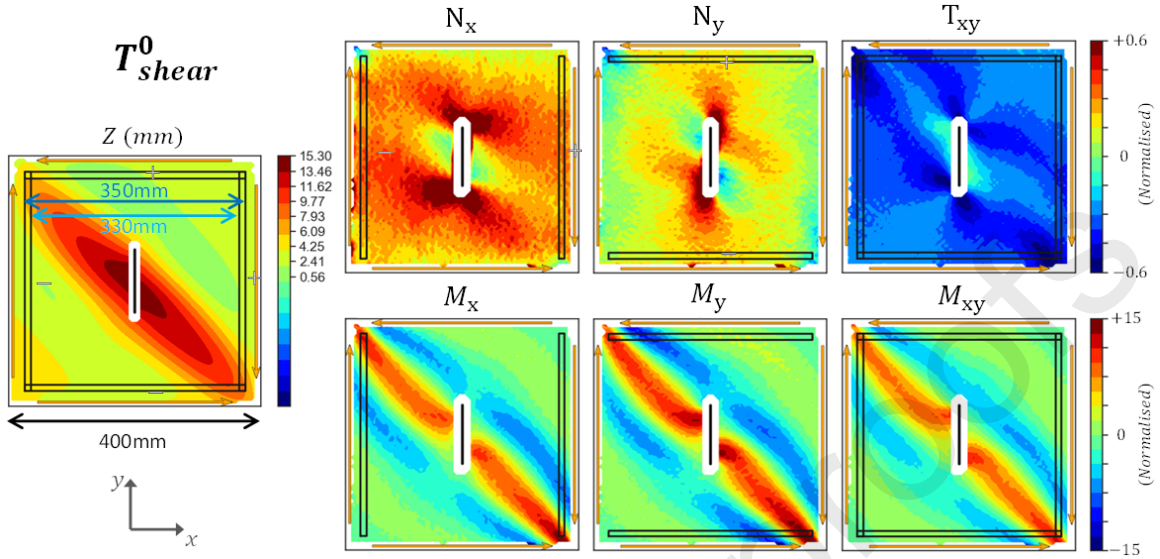

Figure 14: Fields of force and moment fluxes, on the 400 mm ×400 mm area of interest, in the shear test T^0_{shear} between first failure and final failure ($t = 62$ s, see Figure 16). Definition of boxes for spatial averaging of the fields.

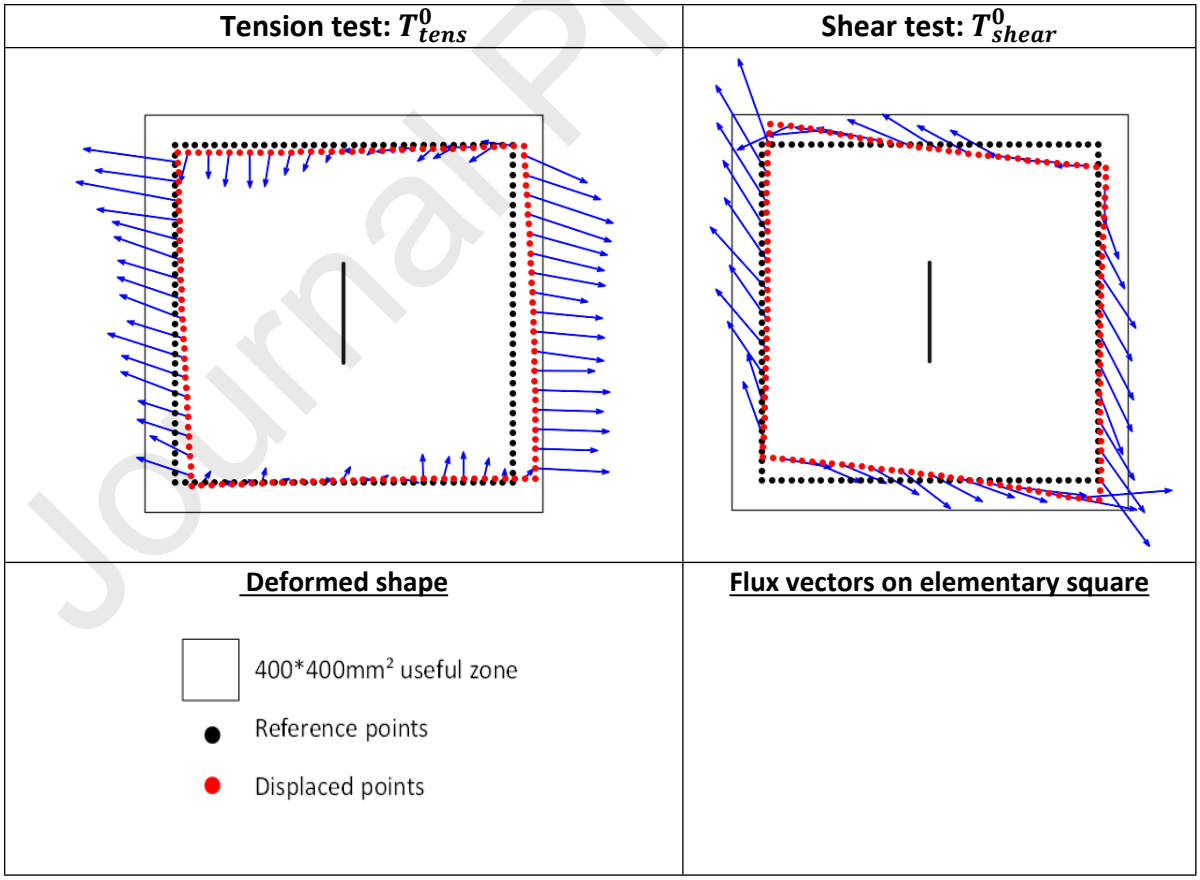

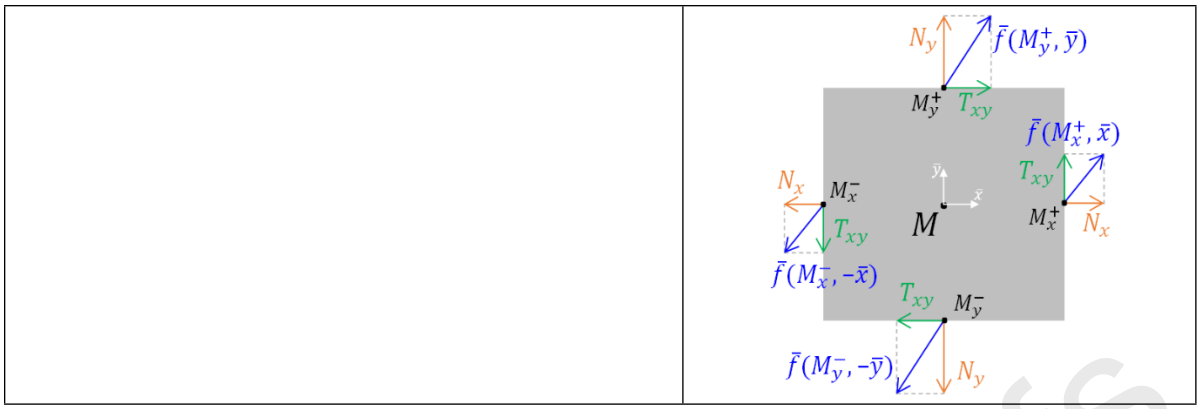

Figure 15: Force flux (blue arrows) shapes obtained with the VERTEX test rig (before first failure).

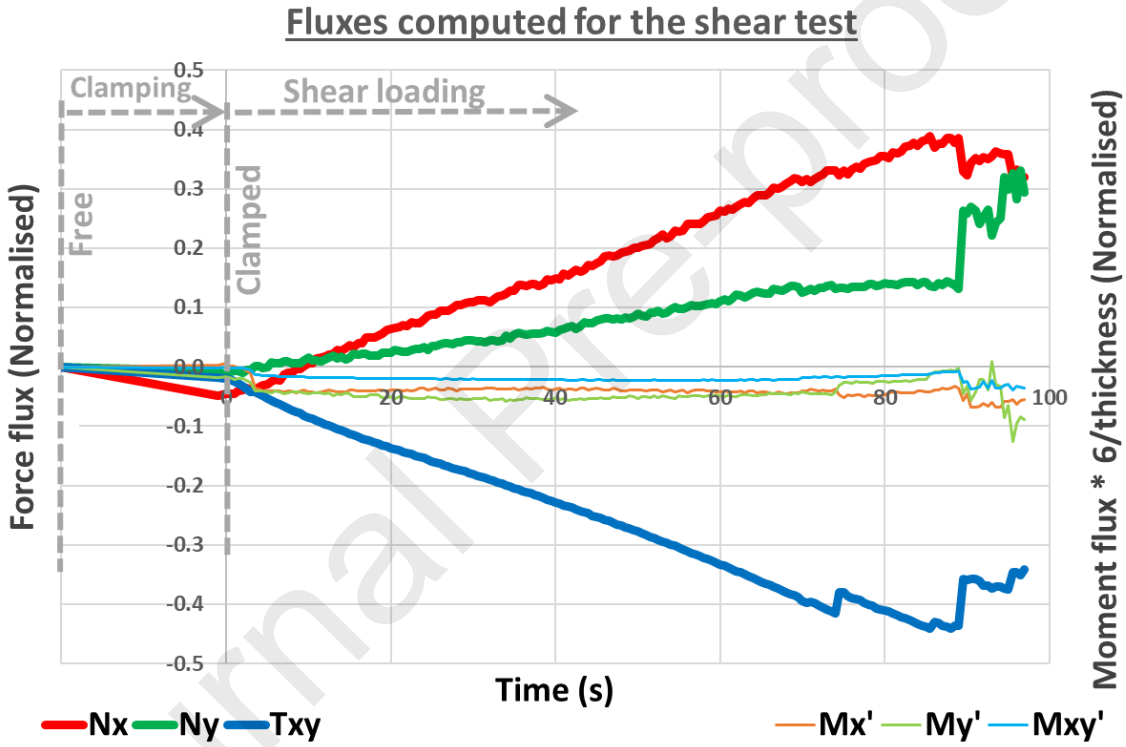

Figure 16: Force and moment fluxes over time for the shear test T^0_{shear}, obtained by spatial averaging of values contained in black boxes of Figure 14.

The tests considered were combinations of pressure, tension and shear, which mostly generated N_x and T_{xy} fluxes as illustrated in Figure 16. Hence, the results shown mainly focus on these in-plane tension and shear fluxes and can be plotted on the same graph for all the tests considered (Figure 17). After the initial clamping and possible pressure application, the fluxes grow progressively according to the load combination imposed by the bench. The tension test T^0_{tens} shows mostly longitudinal tension but also significant shear flux, which has generally been found to be smaller for other tension tests with the VERTEX test rig. It is assumed that, during this test, bolt-hole backlashes of the bench were repositioned from the previous shear test T^{pres}_{shear}, thus generating marginal shear. The shear tests show not only shear flux but also as much tension flux, which is discussed later as the Wagner post-buckling effect. Tests of combined tension and shear gave intermediate results between the two reference loadings. The flux curves are plotted either up to a main failure generating a major loss of load, or up

to the end of proper stereo-correlation because of speckle spalling during crack propagation. Shear force fluxes are negative because jacks 3-4 of the test bench were pushed upward during the tests, as they could not be pulled the opposite way to generate positive shear. Main events, such as first failure, are located on the curves by identifying the first thermal signal on the infrared videos. Identification of the first thermal signal was obvious or very difficult depending on the level of dynamic noise during the test and the magnitude of the first failure. The first infrared failure of the T^{pres}_{tens} test was especially hard to identify and suffered from major uncertainty, since the first thermal signal grew progressively and was only slightly above the noise level.

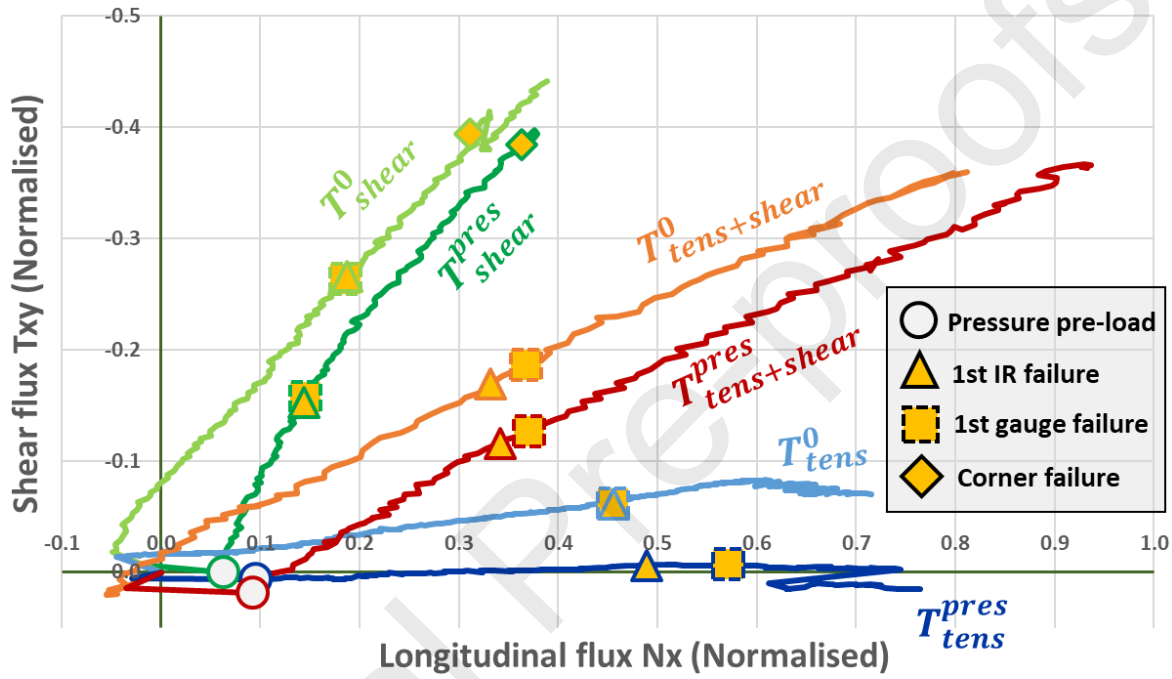

Figure 17: Superposition of computed force flux for each test considered.

3.3 Virtual strain gauges

3.3.1 Global strains

Stereo-correlation gave full-field displacements on the sample and global strains were computed (Equation 3) as the relative average displacement of the sample sides, as if large extensometers had been clipped onto the black boxes shown in Figure 14 [44]. As an alternative to the average flux metric, this also aggregates the complex fields into three scalars representative of the general nature and intensity of loading: ε^{G}_{xx}, ε^{G}_{yy}, ε^{G}_{xy}. Figure 18 plots the global shear strain over the global longitudinal strain for each test considered, so that the evolution of the imposed loading combination can be appreciated throughout each test. This representation is very similar to Figure 17, with global strains progressively increasing after an initial phase of clamping and possible pressure. Note that the shear global strains of T^0_{shear} and T^{pres}_{shear} remain quite pure during the test, whereas the same tests drift into a tension and shear combination on the flux plot. The useful loading does not start from the same point for each test because of clamping variability and pressure. This initial bias mostly persists during the tests, forming a consistent discrepancy between the curves of tests with and without pressure.

$\boldsymbol{x}_-, \boldsymbol{x}_+, \boldsymbol{y}_-, \boldsymbol{y}_+$:four boxes defined in Figure 14

$\boldsymbol{x^0}, \boldsymbol{y^0}$:initial position

$\boldsymbol{u}, \boldsymbol{v}$:displacement along x,y

$\overline{\boldsymbol{u}_{\boldsymbol{y}_-}}$:displacement along x, averaged in the box y_-

$$\boldsymbol{\varepsilon^G_{xx}} = \frac{u_{x+} - u_{x-}}{x^0_{x+} - x^0_{x-}} \qquad \boldsymbol{\varepsilon^G_{yy}} = \frac{v_{y+} - v_{y-}}{y^0_{y+} - y^0_{y-}}$$

$$2 * \boldsymbol{\varepsilon^G_{xy}} = \frac{v_{x+} - v_{x-}}{x^0_{x+} - x^0_{x-}} + \frac{u_{y+} - u_{y-}}{y^0_{y+} - y^0_{y-}}$$

Equation 3: Definition of global strains ε^G_{xx}, ε^G_{yy} and ε^G_{xy}, from the relative displacements of the sample sides.

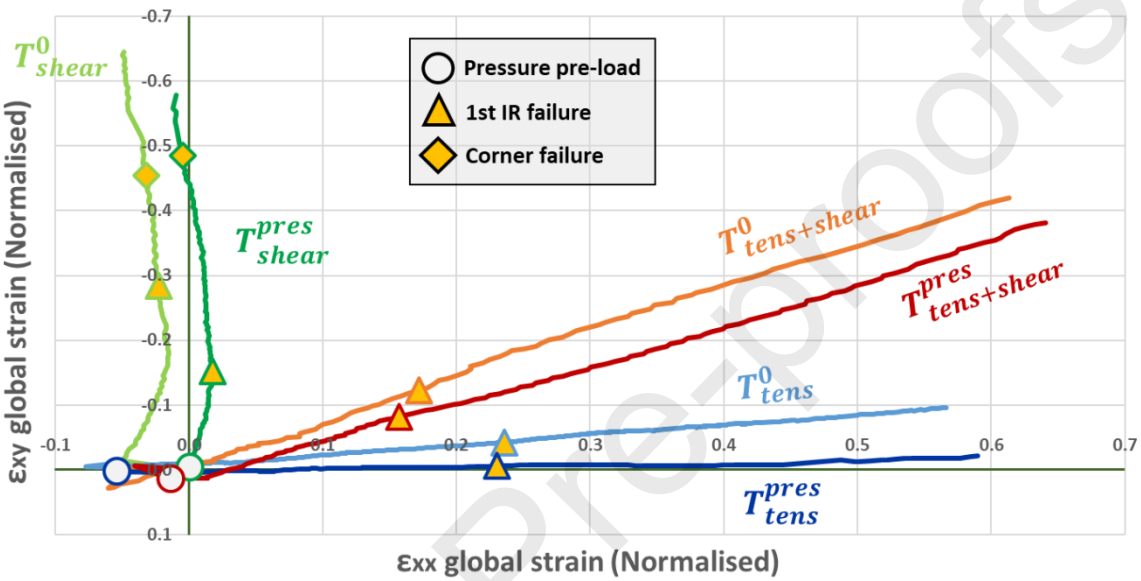

Figure 18: Superposition of computed global strains for each test considered.

3.3.2 Local strains: virtual rosettes at crack tip

Testing on large notches is usually instrumented with an array of rosettes in the direction of the notch after the tip. Stereo-correlation gives strain fields that can be evaluated at any point, which will be referred to as virtual rosette gauges. However, the usual local subset stereo-correlation approach tends to give noisy strains on small subsets or spatially averaged strains on large subsets, which degrades the fidelity required for the local strain concentration at the notch tips.

The tests considered were only instrumented with cameras focusing on the entire area of interest, which did not provide proper quantitative local strain measurements at the notch tip. However, they were good enough for strain jumps to be qualitatively observed (Figure 19). The observation of the first strain jump at $t = 80s$ offers an alternative method for the first failure identification and incidentally matches the previous first failure identification with the infrared method for this test. This method can also lead to unclear or obvious identification depending on the test considered because noise can blur the signal and because the number of fibres involved in the first failures is variable. Figure 17 shows relative positions of first failures identified with the infrared camera and with the virtual gauges: both of which gave very close results except for the T^{pres}_{tens} test, where the first failure was very progressive and thus difficult to identify.

The first strain jump also matches the first tiny cracks that can be observed when zooming in on the notch tip with the visible spectrum cameras; it means that the first visible cracking is, in practice, a

significant multi-ply crack, and not just superficial matrix cracking or speckle spalling. The characteristic size of the virtual gauge considered is 6 mm. Likewise, the common real rosette gauges typically have a length of 6 mm for each directional grid, thus also averaging the measured strains over at least this size. Hence, considering the millimetric scale of strain concentration at the notch tip and the fact that gauges are often placed a few millimetres away from the notch tip, real gauges or the virtual gauges used here give widely averaged values and the absolute quantitative strain they indicate is not to be relied upon. Additional specific cameras focused on the notch tip [42] would be necessary to obtain quantitative strains and spatial refinements finer than those given by real gauges.

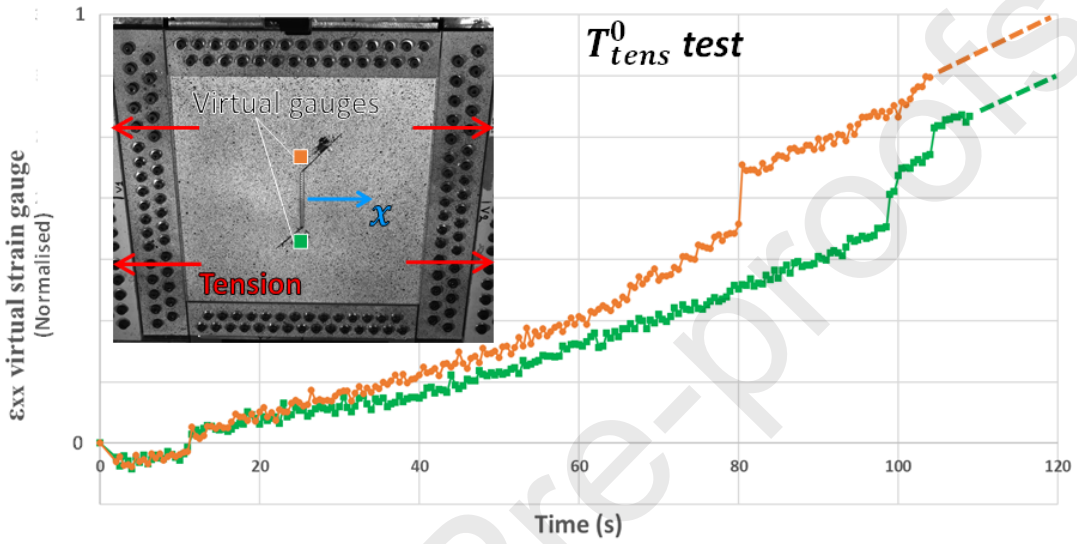

Figure 19: Longitudinal strains plotted over time until signal loss, locally extracted from the stereo-correlation, at 4 mm from the crack tips, on the T^0_{tens} test.

3.4 Equivalent flux and strain

A unique scalar is useful as a metric to describe the loading intensity of the sample, notably to compare loading directions and to plot load intensity evolution on simple 2D graphs. Since the loads were not pure, a single directional force flux or a global strain would not describe the whole loading intensity. An equivalent strain and an equivalent flux are instead computed for each test at each frame, as the quadratic norm of principal values, for the sake of simplicity (Equation 4). The average moment fluxes are ignored because they are relatively much less severe than the force fluxes for the tests considered (Figure 16).

$$(\varepsilon_{xx};\varepsilon_{yy};\varepsilon_{xy}) \quad \Rightarrow \quad (\varepsilon_I;\varepsilon_{II}) \quad \Rightarrow \quad \varepsilon_{eq} = \sqrt{{\varepsilon_I}^2 + {\varepsilon_{II}}^2}$$
$$(N_{xx};N_{yy};T_{xy}) \quad \Rightarrow \quad (N_I;N_{II}) \quad \Rightarrow \quad N_{eq} = \sqrt{{N_I}^2 + {N_{II}}^2}$$

Equation 4: Definition of the equivalent flux/strain, obtained from principal fluxes/strains computed from in-plane strains and force fluxes.

Like the global strains, the equivalent global strain is representative of the displacement imposed on the sample by the bench. Like force fluxes, the equivalent flux is representative of the stress response of the plate to the imposed displacement. Hence, equivalent global strain and flux are, respectively, the mechanical input and output of the plate: Figure 20 plots the equivalent flux against the equivalent global strain to represent the general behaviour of the sample for each test on a single graph. In this (

ε_{eq};N_{eq}) space, all the curves considered are basically linear before the first failure and then they gradually lose stiffness, essentially because of crack propagation.

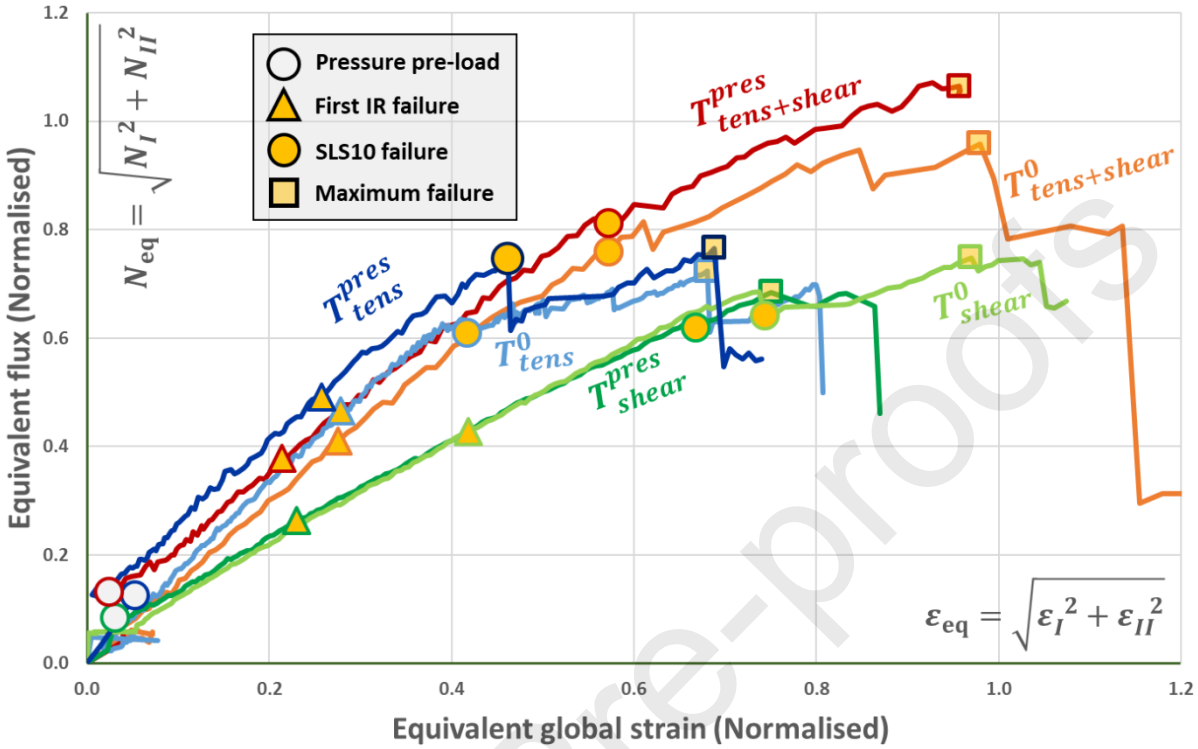

Figure 20: Equivalent flux plotted over the equivalent global strain for all tests.

4 Discussion

4.1 Variability of clamping and pressure

4.1.1 Backlash take-up issue

Clamping introduces loading in the sample since the 128 holes of the sample have to be bolted to the test rig, and the sample holes are not perfectly aligned with the bench holes. After clamping, sample bolt-hole backlashes are set to a new configuration at each test and then repositioned during the test, redistributing the clamping load. This phenomenon can be referred to as backlash take-up, and also affects the thousands of bolted joints of the rig; the initial positions of which are set by the history of the bench and especially by the previous test. Experimentally, this issue is usually dealt with by using a small loading-unloading step to take up the backlashes but this is not as efficient as could be hoped here since: firstly, the take-up of backlashes still occurs up to major loadings and, secondly, the sample contour is entirely bolted to the bench so the loading- unloading would change the sample loading state obtained for the bench reference position.

These issues stem from the action of embedding the sample in the bench structure, with numerous misaligned bolted junctions. This supports the use of measurements taken directly on the sample instead of assuming the loading on the sample from the jack loadings. During the tests considered, the loading was controlled entirely through jack displacements and the fluxes were computed afterwards. To avoid starting the test with a substantial clamping load, a few iterations were possible after clamping to compute fluxes in situ and adjust the reference positions of the jacks to compensate for most of the initial undesired constraints on the sample. The most thorough approach would be to compute the fluxes in real time to correct the jack displacements so that the sample is actually loaded according to the desired force fluxes during the test.

Sample bolts were mostly M8 with rectified shafts of 8.0 mm, and holes in the composite were drilled at 8.3 mm to obtain +0.3 mm clearance to facilitate the cumbersome process of clamping. Increasing this margin could make the bolting easier and reduce the clamping load, in a trade-off among possible undesirable bearing failures. Nevertheless, considering the low loading force applied, it should be beneficial to use a larger clearance for future similar tests.

4.1.2 Quantification of variability of initial conditions

Figure 21 shows the longitudinal and transverse force fluxes, focusing only on the undesired clamping load and on the load induced by the initial pressure application, for each test. All tests start with an assumed zero flux when the samples are simply laid down on the bench, then a single frame is considered to compute the fluxes induced by the clamping (process of bolting the 128 holes of the sample to the bench) and, finally, another single frame is considered to compute the fluxes obtained after the additional pressure for the tests involved.

Practically, clamping causes an N_x^{norm} compressive longitudinal flux between -0.06 and -0.02 but N_y^{norm} transverse flux is substantially lower – between -0.01 and +0.01. Induced shear flux T_{xy}^{norm} is also substantially lower and randomly signed between -0.02 and +0.02. Further studies would be required to know why the longitudinal flux is affected in particular. These values are very low compared with failure fluxes of interest (Figure 17) but are enough to initiate the buckling of the sample before the actual loading. The analytical buckling load of a 400 mm × 400 mm equivalent pristine plate clamped

on four sides is $N_{x\ cr}^{norm} = -0.02$ [58], which is exceeded by the clamping process for all the tests considered.

Pressure set-up fluxes also show variability as the T_{shear}^{pres} shows a flux significantly lower than the other two tests with pressure. Pressure generates both longitudinal and transverse tension but no significant shear flux, as expected given the stacking symmetry.

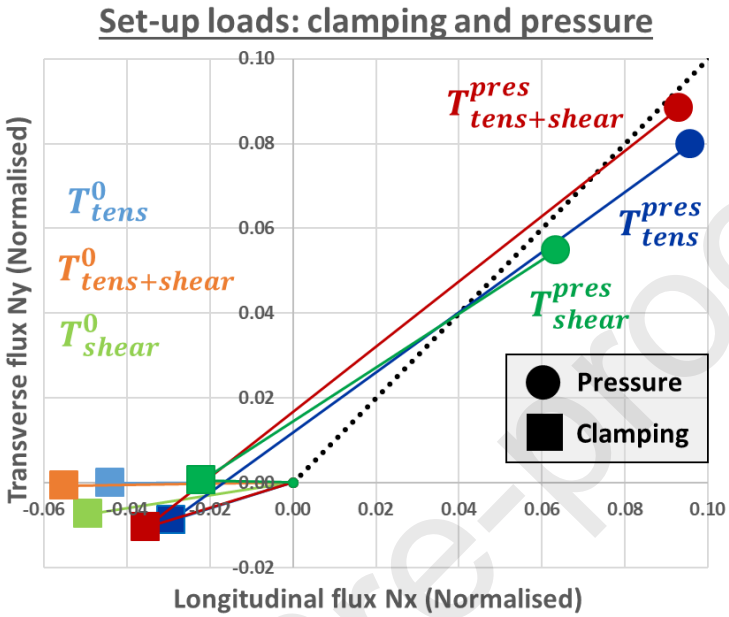

Figure 21 : Initial loadings set up before tests because of clamping and possible pressure.

4.2 Buckling without pressure

4.2.1 Buckling identification

Given the great slenderness of the sample, buckling occurred very early in the test. Moreover, manufacturing defects (internal stresses) generated a slight initial curvature and twisting of a few millimetres, and the sample was generally already buckled before the test, because of the longitudinal compression from clamping. These three reasons explain why it is usually hard or even impossible to identify the point of buckling instability, and why the test is carried out to the far stages of post-buckling.

4.2.2 Tension buckling

Surprisingly, tension test T_{tens}^{0} gave buckling as can be seen in Figure 11 with the out-of-plane position. In a first approach, the longitudinal tension was expected to generate transversal tension as a Poisson effect since the four edges of the sample were clamped. The literature documents the fact that buckling may occur with uniaxial tensile loading if the load is not uniform [59]. However, this tension buckling observed for all VERTEX tension tests is now attributed to a secondary motion of the test bench when the machine is loaded into the tension mode: the flanks of the central box bend towards the centre, generating compression along the transverse direction and thus buckling of the sample. Hence the tests called "tension" were actually biaxial tests with mostly longitudinal tension and some transverse compression (see V displacement fields of the tension test in Figure 11 and Figure 15 - tension).

4.2.3 Shear buckling

Shear buckling is simply explained by the negative shear corresponding to diagonal tension along -45° and the diagonal compression along +45° (Figure 15 – shear and Figure 22). The +45° compression generates perpendicular buckling along the -45° direction. The -45° tension is responsible for the sample tensile failure, generating a perpendicular crack in the +45° direction.

4.3 Shear post-buckling: Wagner effect

Considering the shear equivalence to diagonal tension and compression, the compression along +45° eventually leads to buckling and, thus, to the saturation of the compression load and a buckle along the -45° direction (Figure 22). Imposed shear displacement usually gives proportional pure shear flux but, after buckling, the structure globally produces a combination of longitudinal tension and shear. Since the samples are very slender and initially loaded with clamping or even pressure, they are already buckled before the effective shear loading. Thus, the first phase of pure shear flux cannot be clearly observed and the sample quickly shows a combination of shear and tension (Figure 17), even though the global strain imposed is essentially pure shear (Figure 18). To obtain pure flux-wise shear, proportional compression compensation should be applied by means of actuators 1-2 (Figure 6) but the imposed global strains would then be a combination of shear and compression. This structural shear post-buckling effect is sometimes referred to as the Wagner effect [60] (or "tension diagonal effect") and it illustrates the interest of post-buckling tests.

This effect causes the reorientation of the flux direction, which, depending on the notch length, can be critical for the sample integrity. Alinia et al. [61] studied the buckling and post-buckling of notched panels under shear. They found that crack propagation was especially sensitive to the notch size and orientation, and stated "they can magnify each other and result in extensive loss in load-bearing capacity of shear panels".

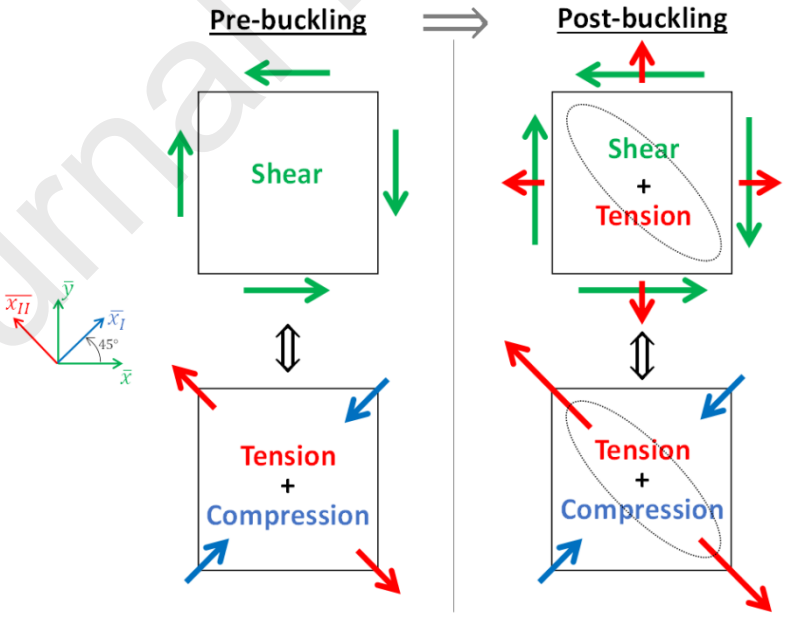

Figure 22: Illustration of the Wagner effect: shear equivalence to diagonal tension/compression and saturation of the compressive flux after buckling.

4.4 Effect of pressure

The internal pressure is applied before the tension/shear loading, thus initially bending the plate upward, generating a maximum deflection of approximately 10 mm (Figure 12). The additional tension/shear only progressively deforms the sample without instability, as the initial pressure cancelled buckling.

The deformed shapes show that the additional pressure simply increases the out-of-plane displacement amplitude without fundamentally altering the blister shape with respect to tests without pressure. The tests considered had only one upward buckle, which directly complied with the upward pressure applied (Figure 12). Past VERTEX tests [43], without pressure on different samples, have occasionally shown downward buckles and even more complex modes that do not properly comply with the upward pressure: pressure addition could lead to the enforcement of an upward buckle on all tests.

The initial pressure introduced substantial force fluxes into the sample (approximately 0.08 for N_x^{norm} and N_y^{norm}, see Figure 21). Figure 17 displays the effect of pressure on the tension/shear loading proportions and on the appearance of the first failure. The loading curves with pressure have an additional tension bias compared to the same tests without pressure. Additional pressure clearly catalyses the first failure for tests with shear (from $T_{xy}^{norm} = -0.27$ for T_{shear}^{0} to $T_{xy}^{norm} = -0.15$ for T_{shear}^{pres}). However, first failure appears later in tension tests with pressure addition but is quantitatively unclear because of the first failure ambiguity during T_{tens}^{pres}.

Pressure on notched panels is often associated with membrane stiffening to compute critical energy release rates locally [27]. For the tests run here, no global stiffening effect due to pressure addition was observed (Figure 20).

4.5 Structural failure

The first failures can be quite easily identified by means of the infrared signal, virtual/real gauges or visible crack propagation, and even in situ with variable difficulties. However, such identification hardly gives quantitative data representative of the severity of the damage or the deteriorated state of the structure. Two criteria are proposed here to quantitatively describe the failed state of the samples.

First, the maximum failure is simply defined as the maximum equivalent flux position during the test. Its identification is trivial (see square symbols in Figure 20 and Figure 24) once the test is carried out up to large damage propagation giving major load drops. Note that $T_{tens+shear}^{pres}$ was stopped a little too early to clearly identify its maximum failure.

Second, a Structural Loss of Stiffness of 10% (referred to as SLS10 failure) is defined to give a quantitative measure of the structural degradation of the sample. Since the loadings are multi-dimensional, the loss of stiffness is evaluated on equivalent flux-strain curves presented in Figure 20, where the first parts of the curves are linear and enable stiffness degradation to be identified easily (Figure 23).

Most curves of Figure 20 are significantly non-linear in the first steps because of the clamping load or the application of the initial pressure. The reference linearity of a given test has to be identified after these initial loads and before the first failure. A second line is plotted with a -10% slope relative to the

first line tangent to the linear section of the test curve. The SLS10 is identified where the second line intersects the test curve, which is clearly after the first failure.

Apart from the actual slight non-linearity of test curves before the first failure, the main limitation of this method is to attribute all the stiffness reduction to material damage when, in fact, it comes partially from elastic non-linearity of the sample. Two thorough methods can untangle the non-linear elasticity from the actual damage: either numerical simulations without failure modelling to estimate the elastic non-linearity, or unloading and reloading of the sample after each significant failure, to consider the initial stiffness degradation.

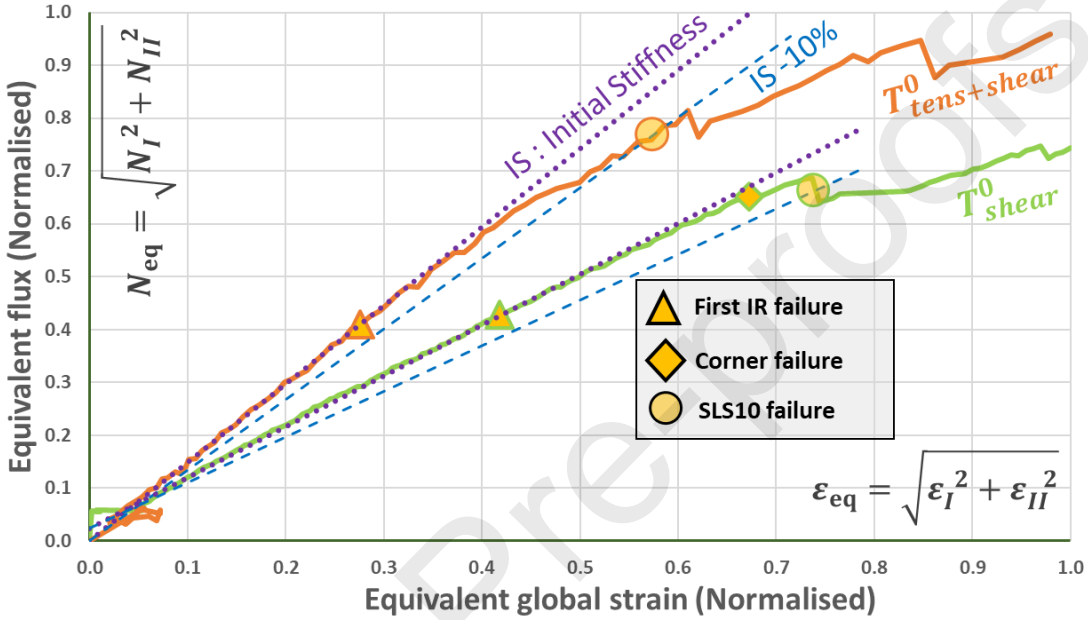

Figure 23: Definition of the SLS10 failure criterion by identification of Structural Loss of Stiffness of 10% on equivalent flux-strain curve.

4.6 Effect of pressure and multi-axiality on failure occurrences

Figure 24 is a recall of Figure 17 with the SLS10 and maximum failures located to visualise their occurrences relatively to the proportions of tension-shear fluxes and their respective magnitudes. Iso-lines of equivalent flux are plotted to enable visual comparison of the intensity of loading of different tension-shear combinations. The N_y flux is ignored in this two-dimensional representation even though it is significant, especially by the transverse tension induced by application of pressure (Figure 21) and by the Wagner effect. Hence, the equivalent flux/strain curves in Figure 20 are more relevant for considering the occurrence of structural failure given the loading intensity, whatever the nature of the loading.

Pressure addition clearly precipitates the first failure for shear tests, but the difference it makes is mitigated for tension+shear and not even significant for tension tests.

Considering SLS10 failures, pressure addition is conservative for tension tests since failure appears later for both flux and strains. However, for shear tests, the structural failure seems to be catalysed by pressure addition but the early corner failure of T^0_{shear} impairs this comparison. Considering maximum failures, the pressure addition gives the same trends as for SLS10 failures.

The effect of loading direction on failure is not clear since shear tests tend to produce failures (first failures and SLS10 failures) not only for somewhat lower equivalent fluxes but also for higher equivalent strains.

Figure 24 starts to delineate the failure envelope for each criterion. Note that, for maximum failures, the typical quarter-elliptical shape of the failure envelope is not respected: tension+shear tests withstand higher tension force fluxes than the tension tests do, suggesting that additional shear flux may make a stabilising contribution.

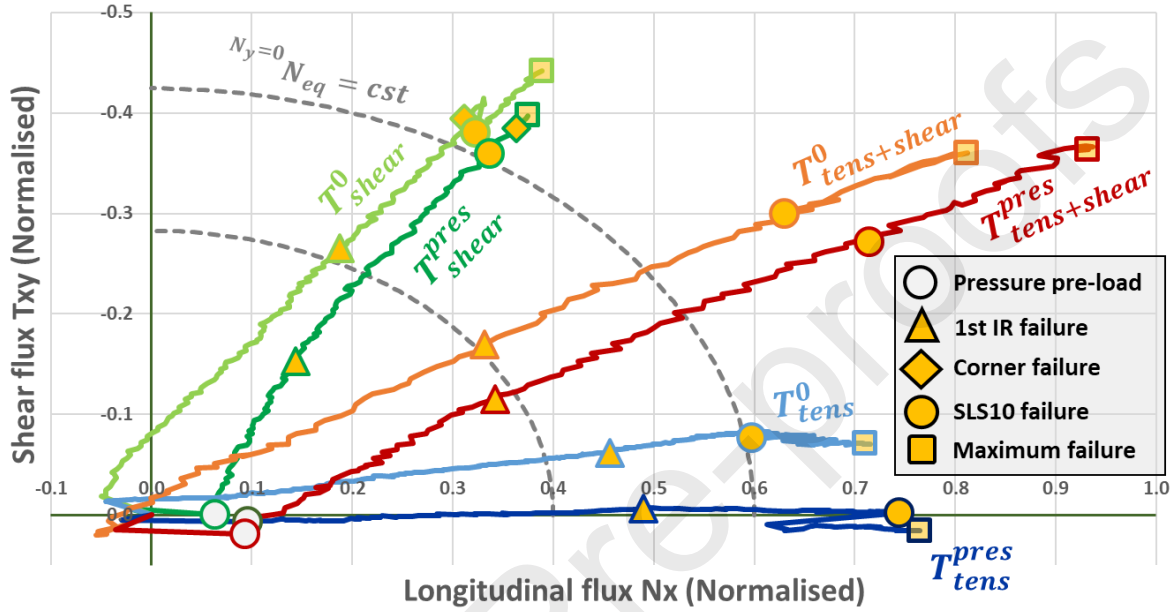

Figure 24: Structural failures located on the force flux curves for each test considered.

4.7 Corner failure

As mentioned above, corner failure occurred during the T^0_{shear} and the T^{pres}_{shear} tests. These failures are indicated with yellow rhombi on the strain/flux curves of Figure 24 and can be seen in the top left corner of the T^0_{shear} thermography of Figure 13.

During the T^0_{shear} test, the corner failure occurred at the beginning of the stiffness degradation and before the structural failures (SLS10 and maximum failures), undermining the validity of the test after this occurrence. Even though this corner failure did not join the central crack directly, it was not an expected failure mode: it may have significantly altered the load distribution and thus subverted the test representativeness of single crack loadings. Considering the T^{pres}_{shear} test, the corner failure happened after the SLS10 failure but before the maximum failure. Thus, corner failure did not affect the test up to SLS10 failure but may have affected it up to maximum failure: depending on the range of interest of the test, i.e. up to the criterion chosen for structural failure, the corner failure may or may not be relevant. The possible interaction of corner failure with structural failures remains to be demonstrated in future studies.

Corner failure is a known issue of multi-axial loading on cruciform samples [35] and is even more difficult to prevent for the tests considered here, where the full sample contour was clamped. In these tests, it is believed that relative displacements of bench parts were responsible for local compression

on the sample, generating the corner failures in the top-left and bottom-right corners. This issue remains to be solved and is still under investigation.

5 Conclusion and perspectives

In this study, six structural tests are considered to evaluate the failure of notched thermoplastic composite panels under combined tension, shear and pressure. Such tests are uncommon in the literature but important to benchmark failure models with realistic loadings.

Unlike coupon or bi-axial tests, those on a sample properly embedded in a larger structure generate more representative loadings of in-flight fuselage sections. However, it is impossible to use actuator displacements and forces as loading indicators for the sample. Flux and strain fields were computed from stereo-correlation to grasp the complexity of the loading spatial distribution. Average and equivalent fluxes and strains were defined to aggregate the complex fields into scalars as a meaningful expression of the loading nature and intensity. Equivalent flux over equivalent global strain allows tests with different types of loading to be compared and thus tackles the loading combination issue, as it enables stiffness evolutions to be superimposed.

The phase of bolting the sample to the test rig led to substantial loading and to buckling of these slender specimens before the actual test. The initial internal pressure essentially bent the sample upward, removing any further buckling instabilities during the test.

The issue of large notch propagation under combined loads was discussed through the observation of post-mortem failure patterns and the identification of various failure criteria: the first failure being evaluated with the first infrared signal of the first strain gauge jump or the first visible crack, and the structural failure evaluated with the SLS10 failure (10% loss of rigidity) or the maximum failure (position of maximum equivalent flux before load dropped).

Pressure addition clearly precipitates the first failure for shear tests but not for tension tests. Considering the effect of pressure on the structural failures, no obvious trend can be identified – notably because of the corner failure of the shear test, which invalidated the end of the test. With or without pressure, shear tests tend to lead to failure for lower equivalent fluxes than tension tests, both for the first failure and for the structural failure.

This work is a first step towards the determination of the effects of the loading type and of the addition of pressure on the structural crack propagation. These intermediate-scale tests with the VERTEX test rig are opening the way towards cost-effective investigation of such structural issues, without the usual complexity and cost of large scale tests.

Ongoing research integrates strong mechanical regularisation within the stereo-correlation algorithm, which gives regular flux fields with very low sensitivity to noise and may later give flux values at borders [62],[42]. Ongoing work is considering non-proportional combined loads to validate the integrity of a whole domain of loading combination with a single test. Future work will focus on scaling up one level of the test pyramid with stiffened samples.

Acknowledgments

This work was funded by the "Fondation Jean-Jacques et Felicia Lopez-Loreta pour l'Excellence Académique" as part of the VIRTUOSE (VIRTUal testing of aerOnautical StructurEs) project (https://websites.isae-supaero.fr/virtuose/).
The academic authors gratefully acknowledge the contribution of Airbus.

6 References

[1] R. Bernatas, S. Dagreou, A. Despax-Ferreres, A. Barasinski, Recycling of fiber reinforced composites with a focus on thermoplastic composites, *Clean. Eng. Technol.* 5 (2021) 100272. https://doi.org/10.1016/j.clet.2021.100272

[2] S. K. Bhudolia, G. Gohel, E. S. B. Subramanyam, K. F. Leong, P. Gerard, Enhanced impact energy absorption and failure characteristics of novel fully thermoplastic and hybrid composite bicycle helmet shells, *Mater. Des* 209 (2021) 110003. https://doi.org/10.1016/j.matdes.2021.110003

[3] S. Z. H. Shah, S. Karuppanan, P. S. M. Megat-Yusoff, Z. Sajid, Impact resistance and damage tolerance of fiber reinforced composites: A review, *Compos. Struct.* 217 (2019) 100-121. https://doi.org/10.1016/j.compstruct.2019.03.021

[4] Y. Carpier, B. Vieille, A. Coppalle, F. Barbe, About the tensile mechanical behaviour of carbon fibers fabrics reinforced thermoplastic composites under very high temperature conditions, *Compos. Part B Eng.* 181 (2020) 107586. https://doi.org/ 10.1016/j.compositesb.2019.107586

[5] B. Vieille, W. Albouy, L. Chevalier, L. Taleb, About the influence of stamping on thermoplastic-based composites for aeronautical applications, *Compos. Part B Eng.* 45:1 (2013) 821-834. https://doi.org/10.1016/j.compositesb.2012.07.047

[6] F. Neveu, C. Cornu, P. Olivier, B. Castanié, Manufacturing and impact behaviour of aeronautic overmolded grid-stiffened thermoplastic carbon plates, *Compos. Struct.* 284 (2022) 115228. https://doi.org/10.1016/j.compstruct.2022.115228

[7] Y. Ma, Y. Yang, T. Sugahara, H. Hamada, A study on the failure behavior and mechanical properties of unidirectional fiber reinforced thermosetting and thermoplastic composites, *Compos. Part B Eng.* 99 (2016) 162-172. https://doi.org/10.1016/j.compositesb.2016.06.005

[8] B. Vieille, J. Aucher, L. Taleb, Comparative study on the behavior of woven-ply reinforced thermoplastic or thermosetting laminates under severe environmental conditions, *Mater. Des.* 35 (2012) 707-719. https://doi.org/10.1016/j.matdes.2011.10.037

[9] S. R. Hallett, B. G. Green, W. G. Jiang, M. R. Wisnom, 2019. An experimental and numerical investigation into the damage mechanisms in notched composites, *Compos. Part Appl. Sci. Manuf.* 40:5 (2009) 613-624. https://doi.org/10.1016/j.compositesa.2009.02.021

[10] D. Mollenhauer, E. V. Larve, R. Kim, B. Langley, Examination of ply cracking in composite laminates with open holes: A moiré interferometric and numerical study, *Compos. Part Appl. Sci. Manuf.*, 37:2 (2006) 282-294. https://doi.org/10.1016/j.compositesa.2005.06.004

[11] J. Serra, C. Bouvet, B. Castanié, C. Petiot, Scaling effect in notched composites: The Discrete Ply Model approach, *Compos. Struct.* 148 (2016) 127-143. https://doi.org/10.1016/j.compstruct.2016.03.062

[12] B. Castanié, S. Crézé, J-J. Barrau, F. Lachaud, L. Risse, Experimental analysis of failures in filled hole compression tests of carbon/epoxy laminates, *Compos. Struct.* 92 (2010) 1192-99. https://doi.org/10.1016/j.compstruct.2009.10.008

[13] P. Chen, Z. Shen, J. Y. Wang, Prediction of the strength of notched fiber-dominated composite laminates, *Compos. Sci. Technol.*, 61 (2001) 1311-21. https://doi.org/10.1016/S0266-3538(01)00030-6

[14] A. R. Torabi, E. Pirhadi, Notch failure in laminated composites under opening mode: The Virtual Isotropic Material Concept, *Compos. Part B Eng.* vol. 172 (2019) 61-75. https://doi.org/10.1016/j.compositesb.2019.05.029

[15] R. Marissen, T. Westphal, J. C. Sterk, Fracture of quasi-isotropic composite sheets with sharp notches, *Compos. Sci. Technol.* 66 (2006) 1803-12 https://doi.org/10.1016/j.compscitech.2005.10.020

[16] J. Serra, C. Bouvet, B. Castanié, C. Petiot, Experimental and numerical analysis of Carbon Fiber Reinforced Polymer notched coupons under tensile loading, *Compos. Struct.* 181 (2017) 145-157. https://doi.org/10.1016/j.compstruct.2017.08.090

[17] X. Xu, M. R. Wisnom, Y. Mahadik, S. R. Hallett, An experimental investigation into size effects in quasi-isotropic carbon/epoxy laminates with sharp and blunt notches, *Compos. Sci. Technol.* 100 (2014) 220-227. https://doi.org/10.1016/j.compscitech.2014.06.002

[18] A. R. Torabi, E. Pirhadi, Extension of the virtual isotropic material concept to mixed mode I/II loading for predicting the last-ply-failure of U-notched glass/epoxy laminated composite specimens, *Compos. Part B Eng.* 176 (2019) 107287. https://doi.org/10.1016/j.compositesb.2019.107287

[19] A. Carpiuc, M. Poncelet, J. Réthoré, S. Roux, CARPIUC benchmark overview: crack advance, reorientation, propagation and initiation under complex loadings, *Adv. Model. Simul. Eng. Sci.* 5:1, (2018) 24. https://doi.org/10.1186/s40323-018-0115-6

[20] N. F. Knight Jr, N. Jaunky, R. E. Lawson, D. R. Ambur, Penetration simulation for uncontained engine debris impact on fuselage-like panels using LS-DYNA, *Finite Elem. Anal. Des.* 36:2 (2000) 99-133. https://doi.org/10.1016/S0168-874X(00)00011-1

[21] X. Xu, S. Takeda, Y. Aoki, S. R. Hallett, M. R. Wisnom, Predicting notched tensile strength of full-scale composite structures from small coupons using fracture mechanics, *Compos. Struct*. 180 (2017). https://doi.org/10.1016/j.compstruct.2017.08.026

[22] J. T. Wang, C. C. Poe, D. R. Ambur, D. W. Sleight, Residual strength prediction of damaged composite fuselage panel with R-curve method, *Compos. Sci. Technol.* 66 (2006) 2557-2565. https://doi.org/10.1016/j.compscitech.2006.01.011

[23] Y. Aoki, S. Takeda, H. Shoji, S. Sugimoto, Y. Iwahori, "Evaluation on discrete source damages of cfrp stiffened panels". *28th International Congress of the Aeronautical Sciences*, Brisbane, 2012. https://www.icas.org/ICAS_ARCHIVE/ICAS2012/PAPERS/866.PDF

[24] M. Remacha, E. Martino, Large damage residual strength analysis: simulations and tests, *ECCM16 - 16th European Conference on Composite Materials*, Seville, Spain, 2014. http://www.escm.eu.org/eccm16/assets/0810.pdf

[25] T. H. Walker,L. B. IIcewia, Tension fracture of laminates for transport fuselage. Part 2: Large notches, *Third NASA Advanced Composites Technology Conference*, Volume 1, Part 2, 1993. https://ntrs.nasa.gov/citations/19950022416

[26] A. Riccio, A. Sellitto, S. Saputo, A. Russo, M. Zarrelli, V. Lopresto, Modelling the damage evolution in notched omega stiffened composite panels under compression, *Compos. Part B Eng.* 126 (2017). https://doi.org/10.1016/j.compositesb.2017.05.067

[27] J. Wang, C. Lotts, D. Sleight. Analysis of discrete-source damage progression in a tensile stiffened composite panel. *40th Structures, Structural Dynamics, and Materials Conference and Exhibit*, St. Louis, MO ,U.S.A. 1999. https://doi.org/10.2514/6.1999-1336

[28] A. Bergan, J. Bakuckas, J. Awerbuch, T.-M. Tan, Assessment of damage containment features of a full-scale PRSEUS fuselage panel, *Compos. Struct.* 113 (2014) 174‑185. https://doi.org/10.1016/j.compstruct.2014.03.011

[29] E. Oterkus, E. Madenci, O. Weckner, S. Silling, P. Bogert, A. Tessler, Combined finite element and peridynamic analyses for predicting failure in a stiffened composite curved panel with a central slot, *Compos. Struct.*, 94 (2012) 839‑850. https://doi.org/10.1016/j.compstruct.2011.07.019

[30] D. R. Ambur, M. Rouse, Design and Evaluation of Composite Fuselage Panels Subjected to Combined Loading Conditions, *J. Aircr.* 42 (2005) 1037‑1045, https://doi.org/10.2514/1.18994

[31] S. Laustsen, E. Lund, L. Kühlmeier, O. Thomsen, Failure behaviour of grid-scored foam cored composite sandwich panels for wind turbine blades subjected to realistic multiaxial loading condition', *J. Sandw. Struct. Mater.*, vol. 16, no. 5, pp. 481–510, 2014. https://doi.org/10.1177/1099636214541367

[32] R. A. Fields, W. L. Richards, M. V. DeAngelis, Combined Loads Test Fixture for Thermal-Structural Testing Aerospace Vehicle Panel Concepts, H-2488, 2004. https://ntrs.nasa.gov/citations/20040031531

[33] M. Rouse, D. Anbur, Fuselage response simulation of stiffened panels using a pressure-box test machine, *36th Structures Structural Dynamics and Materials Conference*, New Orleans, LA, U.S.A., 1995. https://doi.org/10.2514/6.1995-1362

[34] A. Bergan, J. Bakuckas, J. Awerbuch, T.-M. Tan, Assessment of damage containment features of a full-scale PRSEUS fuselage panel, *Compos. Struct.*, vol. 113, pp. 174–185. 2014. https://doi.org/10.1016/j.compstruct.2014.03.011

[35] P. Hopgood, J. Cook, A. Clarke, Multi-axial testing of planar composite specimens, *Proc. 12th Int. Conf. Compos. Mater. Paris Fr.*, 1999. http://iccm-central.org/Proceedings/ICCM12proceedings/site/papers/pap792.pdf

[36] R. W. Peters, Buckling tests of flat rectangular plates under combined shear and longitudinal compression, 1946. https://ntrs.nasa.gov/api/citations/19930082377/downloads/19930082377.pdf

[37] H. Klein, General buckling tests with thin-walled shells. Report DLR-Mitt, 1989.

[38] G. Zucco, V. Oliveri, M. Rouhi, R. Telford, G. Clancy, C. McHale, R. O'Higgins, T.M. Young, P.M. Weaver, D. Peeters, Static test of a variable stiffness thermoplastic composite wingbox under shear, bending and torsion, *The Aeronaut. J.* 124:275 (2020) 635-666. https://doi.org/10.1017/aer.2019.161

[39] National Airlines Flight 27 incident, https://en.wikipedia.org/wiki/National_Airlines_Flight_27

[40] A. Bergan, C.G. Dávila, F. Leone, J. Awerbuch, T.-M. Tan, An Analysis Methodology to Predict Damage Propagation in Notched Composite Fuselage Structures, SAMPE, Baltimore, 2015. https://ntrs.nasa.gov/citations/20160007429

[41] J. Rouchon, Certification of large airplane composite structures, *28th International Congress of the Aeronautical Sciences*, Stockholm, 1990. https://www.icas.org/ICAS_ARCHIVE/ICAS1990/ICAS-90-1.8.1.pdf

[42] J. Serra, J. E. Pierré, J. C. Passieux, J. N. Périé, C. Bouvet, B. Castanié, Validation and modeling of aeronautical composite structures subjected to combined loadings: The VERTEX project. Part 1: Experimental setup, FE-DIC instrumentation and procedures , *Compos. Struct.* 179 (2017) 224-244. https://doi.org/10.1016/j.compstruct.2017.07.080

[43] J. Serra, J. E. Pierré, J. C. Passieux, J. N. Périé, C. Bouvet, B. Castanié, C. Petiot, Validation and modeling of aeronautical composite structures subjected to combined loadings: The VERTEX project. Part 2: Load envelopes for the assessment of panels with large notches, *Compos. Struct.* 180 (2017) 550–567. https://doi.org/10.1016/j.compstruct.2017.08.055

[44] A. Trellu, G. Pichon, C. Bouvet, S. Rivallant, B. Castanié, J. Serra, L. Ratsifandrihana, Combined loadings after medium velocity impact on large CFRP laminate plates: Tests and enhanced computation/testing dialogue, *Compos. Sci. Technol.* 196 (2020) 108194. https://doi.org/10.1016/j.compscitech.2020.108194

[45] Wolf, K., Kossira, H., An Efficient Test Method for the Experimental Investigation of the Post-buckling Behavior of Curved Shear Panels, *ECCM Composite Testing and Standardization, Amsterdam*, 1992.

[46] Romeo, G. and Frulla, G., Buckling and Post-buckling behavior of Anisotropic Plates Under Combined Biaxial Compression and Shear Loads, *ECCM Composite Testing and Standardization, Amsterdam*, 1992.

[47] Rouse, M., Young, R.D., Gehrki, R.E., Structural Stability of a Stiffened Aluminum Fuselage Panel Subjected to Combined Mechanical and Internal Pressure Loads, AIAA 2003-1423, *44th AIAA/ASME/ASCE/AHS/ASC Structures, Structural Dynamics, and Materials Conference*, Norfolk, VA, 2003.

[48] A. Bergan, J. G. Bakuckas, A.E Lovejoy, D.C. Jegley, K. A. Linton, G. Korkosz, J. Awerbuch, T-M. Tan, Full-Scale Test and Analysis of a PRSEUS Fuselage Panel to Assess Damage-Containment Features, *2011 Aircraft Airworthiness and Sustainment (AAS) Conference*, San Diego, 2011. https://ntrs.nasa.gov/citations/20110011134

[49] G. Zucco, V. Oliveri, D. Peeters, R. Telford, G. J. Clancy, C. McHale, M.Rouhi, R. O'Higgins, T. M. Young, P.M. Weaver, Static Test of a Thermoplastic Composite Wingbox Under Shear and Bending Moment, AIAA/ASCE/AHS/ASC *Structures, Structural Dynamics, and Materials Conference, Kissimmee*, Florida, 2018. https://doi.org/10.2514/6.2018-0482

[50] G. R. K. Prasad,R. F. Mohammad, Effect of ply orientation, staking sequence and notch geometry on the failure behaviour of glass fibre-reinforced epoxy composite laminates: A numerical investigation. *IOP Conf. Ser. Mater. Sci. Eng.*, 1225 (2022) 012003. https://doi.org/10.1088/1757-899X/1225/1/012003

[51] E. T. M. Krämer, W. J. B. Grouve, L. L. Warnet, S. Koussios, R. Akkerman, Tool-ply interaction in the formation of waviness during C/PEEK consolidation, *Compos. Part Appl. Sci. Manuf.* 144 (2021) 106327. https://doi.org/10.1016/j.compositesa.2021.106327

[52] T. Choupin, L. Debertrand, B. Fayolle, G. Régnier, C. Paris, J. Cinquin, B. Brulé, Influence of thermal history on the mechanical properties of poly(ether ketone ketone) copolymers, *Polym. Cryst.* 2:6 (2019) 10086. https://doi.org/10.1002/pcr2.10086

[53] B. Castanié, J. J. Barrau, J. P. Jaouen, S. Rivallant. Combined shear/compression structural testing of asymmetric sandwich structures, *Exp. Mech.* 44:5 (2004) 461–472. https://doi.org/10.1177/0014485104047607

[54] B. Castanié, J. J. Barrau, J. P. Jaouen, Theoretical and experimental analysis of asymmetric sandwich structures, *Compos. Struct.* 55:3 (2002) 295–306. https://doi.org/10.1016/S0263-8223(01)00156-8

[55] T. Lisle, C. Bouvet, N. Hongkarnjanakul, M.-L. Pastor, S. Rivallant, P. Margueres, Measure of fracture toughness of compressive fiber failure in composite structures using infrared thermography, *Compos. Sci. Technol.*, 112 (2015) 22‑33. https://doi.org/10.1016/j.compscitech.2015.03.005

[56] C. Bouvet, Mechanics of aeronautical composite materials. WILEY, 2017.

[57] Z. Yang, D. Chen, L. Zhou, Y. Gao, Study on stress distribution of multilayer steel wire wound hose under the condition of oil pressure, in *2016 12th IEEE/ASME International Conference on Mechatronic and Embedded Systems and Applications (MESA)*, 2016. https://doi.org/10.1109/MESA.2016.7587114

[58] EDSU, Buckling of rectangular specially orthotropic plates. 1995. http://www.esdu.com

[59] A. W. Leissa, E. F. Ayoub, Tension Buckling of Rectangular Sheets Due to Concentrated Forces, *J. Eng. Mech.*, 115 (1989) 2749‑2762. https://doi.org/10.1061/(ASCE)0733-9399(1989)115:12(2749)

[60] H. Wagner, Structures of thin sheet metal their design and construction, *NACA Memo 490*, 1928. https://ntrs.nasa.gov/api/citations/19930090854/downloads/19930090854.pdf

[61] M. M. Alinia, S. A. A. Hosseinzadeh, H. R. Habashi, Influence of central cracks on buckling and post-buckling behaviour of shear panels, *Thin-Walled Struct.*45:4 (2007) 422‑431. https://doi.org/10.1016/j.tws.2007.03.003

[62] J.-E. Pierré, J.-C. Passieux, J.-N. Périé, Finite Element Stereo Digital Image Correlation: Framework and Mechanical Regularization, *Exp. Mech.* 57:3 (2017) 443-456. https://doi.org/10.1007/s11340-016-0246-y

Highlights

CFRP thermoplastic large specimens with large notches are tested

The VERTEX test is used to apply combined loadings of tension, shear and internal pressure.

Failure scenarii are identified thanks to DIC (6 cameras) and infrared cameras

Failure scenarii are discussed

Declaration of interests

☒ The authors declare that they have no known competing financial interests or personal relationships that could have appeared to influence the work reported in this paper.

☐The authors declare the following financial interests/personal relationships which may be considered as potential competing interests:

Florent Grotto , Christophe Bouvet , Bruno Castanié , Joël Serra